HAL
archives-ouvertes.fr

C-O-H fluid solubility in Haplo-basalt under reducing conditions: An experimental study

Yann Morizet, M. Paris, Fabrice Gaillard, Bruno Scaillet

▶ To cite this version:

HAL Id: insu-00524494

https://hal-insu.archives-ouvertes.fr/insu-00524494

Submitted on 8 Oct 2010

C-O-H FLUID SOLUBILITY IN HAPLO-BASALT UNDER REDUCING CONDITIONS: AN EXPERIMENTAL STUDY

Y. MORIZET[1], M. PARIS[2], F. GAILLARD[3], B. SCAILLET[3]

[1] Université de Nantes, Nantes Atlantique Universités, Laboratoire de Planétologie et Géodynamique de Nantes (LPGN)

UMR CNRS 6112

2 rue de la Houssinière, 44322 NANTES (France)

[2] Institut des Matériaux Jean Rouxel (IMN), Université de Nantes

UMR CNRS 6502

2 rue de la Houssinière, BP32229, 44322 NANTES Cedex 3 (France)

[3] CNRS/INSU-Université d'Orléans-Université François Rabelais Tours

UMR 6113

Institut des Sciences de la Terre d'Orléans

1a rue de la Férollerie, 45071, Orléans, France

Corresponding author: Dr Yann Morizet

Permanent address:

Laboratoire de Planétologie et Géodynamique de Nantes (LPGN), Université de Nantes

CNRS/INSU – UMR CNRS 6112

2 rue de la Houssinière, BP 92208.

44322 Nantes Cedex 3 (FRANCE).

Email: yann.morizet@univ-nantes.fr

Tel: +33 (0) 2 5112 5491

Fax: +33 (0) 2 5112 5268

Abstract:

We conducted an experimental study to constrain the C-H-O solubility and speciation in hydrous silicate melts equilibrated under reduced fO_2 conditions. Haplo-basaltic glasses in the NCMAS-C-O-H system were synthesised using IHPV at 1250°C, 200-300 MPa with variable applied fH_2 so as to vary fO_2. Recovered rapidly quenched glasses were characterized using various spectroscopic methods: Micro-FTIR, Raman and ^{13}C-MAS NMR. Glass CO_2 content changes from 680 to 1320 ppm between ΔFMQ-2.6 and ΔFMQ+2.6 independently of H_2O content changing from 1.3 to 4.0 wt.%. Recent thermodynamic modelling of isobaric CO_2-H_2O solubility fails to reproduce our CO_2-H_2O solubility trend under reducing conditions. The lower CO_2 solubility in the melt as compared to more oxidized conditions is directly correlated to the decrease of fCO_2 within the fluid phase under reducing conditions. Carbonate groups (CO_3^{2-}), OH^- and H_2O^{mol} are the volatile species in the glasses. No evidence for CH_4, carbides or organic compounds was observed. ^{13}C MAS NMR analysis suggests that several carbonate units are coexisting in the glasses. $\{^1H\}$ ^{13}C-CPMAS NMR suggests that all CO_3^{2-} units are surrounded by OH groups. Those environments appear to slightly change with changing fO_2 conditions suggesting different degree of hydrogenation in the vicinity of the carbonate groups. Our data show that the presence of a significant amount of dissolved does not increase the solubility of species such as CO or CH_4. In other words, such species remain insoluble in basaltic melts, as established under dry conditions. Altogether, our CO_2 solubility results show that a wet but reduced basalt will degass more C-species than if oxidized, owing to the lower prevailing fCO_2 and insoluble character of

3

CO. The presence of an important fraction of CO in the fluid phase will have a large

impact on the primitive atmospheric compositions of Mars and the Earth.

1. Introduction:

Earth degassing through volcanism is an important process to investigate for understanding the chemical variations of our atmosphere and the impact of volcanism on climate change. Establishing reliable models of the carbon and hydrogen geochemical cycles within planetary bodies such as Mars and the Earth implies understanding the partitioning of carbon and hydrogen species between their internal reservoirs. Earth's mantle is one of the most important carbon and hydrogen reservoir of the Earth (e.g. Javoy et al., 1986; Marty and Jambon, 1987; Ahrens, 1989; Ingrin et al., 1995; Sleep and Zahnle, 2001; Gaillard et al., 2008), being in particular, one of the most important carbon dioxide (CO_2) long term source for the atmosphere (e.g. Zhang and Zindler, 1989; Azbel and Tolstikhin, 1990).

Under oxidising conditions, CO_2 and H_2O are the most abundant species to be dissolved in silicate melts. H_2O and CO_2 solubility, speciation and dissolution mechanisms are fairly well constrained as a function of melt composition, temperature, pressure (e.g. Fogel and Rutherford, 1990; Thibault and Holloway, 1994; Dixon, 1997; Morizet et al., 2002; Behrens et al., 2004; Moore, 2008). CO_2 and H_2O gases are presently the two most important volatiles released by Earth degassing through volcanism however more reduced species such as CH_4 and CO are thought to have been degassed especially during the Archean period giving rise to a more reduced atmosphere (Kump and Barley, 2007; Kump, 2008). The impact of those reduced species on the global environmental change for the primitive atmospheres is to be considered.

Determining the solubility behaviour of C-H-O volatiles in reduced magmas is essential also for constraining the global geochemical cycle of those volatiles during the evolution

of other terrestrial planets such as Mars (e.g., Hirschmann and Withers, 2008; Gaillard and Scaillet, 2009). There is unfortunately currently little information on the solubility and speciation behaviour of reduced C-H-O species in silicate melts, in particular under H_2O-rich conditions which may have prevailed during the early magma ocean stage (e.g., Drake and Righter, 2002; Righter et al., 2007; Elkins-Tanton, 2008).

Experimental data were acquired by Pawley et al. (1992) for basaltic glasses: these authors demonstrated that the relationship between CO_2 solubility and CO_2 fugacity (fCO_2) established at high fO_2 is valid as well under reduced conditions in the low pressure range investigated (<150 MPa). Kadik et al. (2004) presented additional results for the solubility, speciation and dissolution mechanisms of C-O-H fluids in silicate glasses as a function of redox conditions suggesting the presence of more reduced species such as CH_4 dissolved within the melt. At high pressure (1.0-2.5 GPa) and under reducing conditions (iron-wüstite buffer), for glasses in the Na_2O-SiO_2 system, Mysen et al. (2009) proposed the formation of methyl groups (CH_3) bound to Non-Bridging Oxygens (NBO) suggesting the depolymerization of the melt through the formation of C-H bonds. Notwithstanding, there is no clear evidence as to whether or not a reduced fluid depolymerizes the melt structure.

We have conducted an experimental study aimed at determining the solubility, speciation and dissolution mechanisms for C-H-O fluid species in equilibrium with a synthetic hydrous basaltic melt synthesised at 200-300 MPa and 1250°C. Experiments were conducted under various redox conditions from ΔFMQ+2.6 to -2.6, i.e. outside the graphite saturation surface. All experiments were performed under hydrous conditions as compared to previous studies (e.g., Pawley et al., 1992). Results on solubility and

6

speciation for C-H-O species were obtained from spectroscopic analyses. An approach is
proposed for the dissolution mechanisms for C-H-O species.

2. Experimental and analytical methods:

2.1. Experimental synthesis:

Synthetic Fe-free basaltic starting composition was prepared from a mixture of oxides
(SiO_2, Al_2O_3 and MgO) and carbonates ($Na_2{}^{13}CO_3$ and $Ca^{12}CO_3$). The absence of iron is
justified by the analytical needs for investigating the C speciation with NMR which
cannot be used on Fe-bearing materials. The investigated composition is 54.8 wt.% SiO_2,
21.1 wt.% Al_2O_3, 8.1 wt.% MgO, 12.9 wt.% CaO and 3.2 wt.% Na_2O. It corresponds to
an $NBO/T = 0.42$ (Non-Bridging Oxygen / Tetrahedral charges) according to the
definition of Mysen (1988; 1990). The starting composition has an Aluminium Saturation
Index $ASI = 0.73$ following the definition of London (1992).

The sample nomenclature is explained as follows: the first figure stands for the
experiment number, the second figure stands for the capsule number during the
experiment and the final part gives some particularity of the sample (e.g. *us*:
undersaturated; *ox*: for the most oxidized sample; *red*: for the most reduced sample).

The starting composition was prepared as follows:

1) SiO_2, Al_2O_3, MgO and $Ca^{12}CO_3$ were mixed together and held at 1300°C
   for few hours in order to dissociate the calcium carbonate. $^{12}CO_2$ is
   degassed during this process, however it appears to be an incomplete
   decarbonation as ^{12}C isotope is still present within the glass (see section
   4.1).

2) $Na_2{}^{13}CO_3$ (except for run 2-2-^{12}C and 3-2-^{12}C in which $Na_2{}^{12}CO_3$ was

added, see Table 1) is added to complete the composition and is the source

of both CO_2 (~1 wt.%) during the experiment and ^{13}C-source for solid-

state NMR analytical needs. Under the studied P,T conditions (200-300

MPa, 1250°C), the 1 wt.% $^{13}CO_2$ added to the staring composition is well

above the solubility saturation level for basaltic compositions (Fine and

Stolper, 1986; Pan et al., 1991; Dixon et al., 1995) and the melt will be in

equilibrium with an excess fluid phase in which C-species dominate.

3) A small proportion of Fe_2O_3 (< 1 wt.%) is added as a source of

paramagnetic element to reduce the NMR acquisition time length by

reducing the relaxation time (Maekawa et al., 1991) which is usually long

for ^{13}C nuclei (Kohn et al., 1991). The FeO^{tot} was quantified by electron

microprobe and is reported in Table 2 along with the NMR analytical

conditions. Except for 6-1-*ox*, the FeO^{tot} measured value in the starting

materials were below 0.6 wt.% which is recognized not to produce a

drastic change in the NMR spectrum profile (Maekawa et al., 1991). For

6-1-*ox*, the FeO^{tot} is relatively high due to high fO_2 that minimize Fe loss

toward the container and is likely to produce changes in the line shape of

the NMR spectrum.

A particular case is made for 4-2-*us* which is initially CO_2-free. The starting composition

was prepared by mixing all oxides and carbonates and firing the mixture at 1300°C for

$^{12}CO_2$ decarbonation.

Between 0 and 4 wt.% H_2O is added together with the solid starting materials in the platinum capsules (see Table 1). Starting composition is loaded after water and the platinum capsule is welded shut. Experiments are conducted in an Internally Heated Pressure Vessel (IHPV) for run durations between 2 to 3 hours which is sufficient to ensure chemical equilibrium is achieved throughout the sample charge considering that at 1250ºC 1) CO_2 and H_2O diffusion coefficient are high (Watson, 1994; Zhang et al., 2007) and 2) H_2 diffuses very quickly through the sample charge (Schmidt et al., 1997; Gaillard et al., 2003a).

The experimental conditions are conducted between 197 and 320 MPa for pressure, 1250°C for temperature (see Table 1 for detailed experimental conditions). All recovered synthesised samples are listed in Table 1.

The procedure to achieve the experimental conditions is described elsewhere (e.g., Scaillet et al., 1992) and is summarized as follow. The IHPV is first loaded at room temperature with a known partial pressure of pure H_2, Argon gas is then loaded up to roughly half the desired total pressure (P^{tot}) value (either 100 or 150 MPa). The temperature is then brought to the final value and the P^{tot} increases up to requested experimental pressure (200 or 300 MPa). P and T are constantly monitored during the experiment using an electronic gauge for P and a type S thermocouple connected to a Eurotherm controller for T. The T change along the capsule is measured with an additional thermocouple and does not exceed 15ºC. P, T measurements are accurate within ± 20 bars and ± 5ºC.

The estimate of the final $P(H_2)$ (see Table 1) during the experiment is crucial. The high temperature of the experiment and the short run duration prevent the use of techniques

allowing direct measurements of the $P(H_2)$ such as the Shaw membrane ($Ag_{40}Pd_{60}$, Scaillet et al., 1992) or the solid buffer (Eugster and Wones, 1962). An internal calibration completed over more than 10 years of experiments in the H_2-Ar gas mixture with the same autoclave shows that under those P-T conditions the final estimated $P(H_2)$ is therefore equivalent to roughly 3-4 times the initial loaded $P(H_2)$ (Martel et al., 1999; Gaillard et al., 2003b; Di Carlo et al., 2006). The final $P(H_2)$ experienced during the run are shown in Table 1, using an empirical multiplication factor of 3. Changing the multiplication factor to 4 will only slightly affect the final calculated fO_2 value, by -0.3 log unit in our study.

Hydrogen acts as a reducing agent for the loaded CO_2 according to the reaction in the fluid phase:

$$CO_2^{fl} + H_2^{fl} \leftrightarrow CO^{fl} + H_2O^{m} \qquad (1)$$
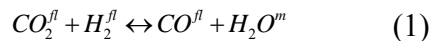
where fl stands for the gas in the fluid phase and m stands for the species in the melt phase. Further reduction might produce more reduced species such as CH_4 (Holloway, 1987) or even graphite.

The sample is quenched to the ambient temperature by dropping the capsules into the cold part of the IHPV. The quench rate is relatively fast, on the order of 150°C/s for that kind of apparatus (Di Carlo et al., 2006; Iacono-Marziano et al., 2008). In all cases, opening of the capsules produced a hiss suggesting that a fluid phase was present in the capsule during the experiment.

Several chips from the recovered glasses were selected for micro-Raman and micro-FTIR analyses. The remaining of the glass sample was then crushed for ^{13}C-MAS NMR analysis. Optical examination of the glass reveals the presence of randomly distributed round shaped fluid inclusions as shown in Morizet et al. (2009). The recovered glasses are free of crystals. For the most reduced samples, the glass is not totally transparent although not blackened. We carefully scrutinized the sample but did not get evidence for graphite crystalline phase however platinum complexes might have been formed during the experiments. Our observation is also confirmed by the absence of i) Raman signatures for graphite either within the glass or the fluid inclusion walls and ii) ^{13}C-NMR signatures for crystalline or amorphous graphite.

2.2. Confocal Micro-Raman:

Confocal micro-Raman was used to characterize i) the fluid species inside inclusions for determining the fO_2 experienced during the run (see Table 1 for numerical values, log fO_2 (2); and section 3 for calculation description) and ii) the H_2O in the melt via the silicate and water-related Raman signatures (see Table 3 for numerical values, H_2O^{tot} (2)). The Raman system is a Jobin-Yvon Labram spectrometer (focal distance = 300 mm) equipped with a 2400 gratings/mm CCD detector. The light source is an Ar laser Innova 300-5W from Coherent© operating at 514.5 nm. The typical output laser power was set to 120 mW. The analyses were performed in confocal mode (hole = 500 μm, slit = 200 μm) with an Olympus (x50) objective. The confocal mode is particularly useful for fluid inclusion analysis as the contribution of the surrounding glass is reduced in the final spectrum.

Spectra were recorded between 200 and 4000 cm^{-1}. Fluid inclusions were analysed for CO_2-CO scattering between 1100 and 2200 cm^{-1}. Analyses were also done in the CH_4 region (2900 cm^{-1}) to check its presence. The network vibrational modes were characterized in the 200-1200 cm^{-1} range and the OH stretching band in the 2700-3800 cm^{-1} range. The spectral frequency position was measured with the emission lines of Ne- and Hg-lamps. The accuracy stays within ±1 cm^{-1}.

The acquisition time for the different phases (glass and fluid inclusions) is relatively short and is usually within 20-30 s to obtain a reasonably good signal to noise ratio (S/N). All spectra are normalised to the same acquisition time for relevant quantification.

2.3. Micro-FTIR:

Doubly polished plates were prepared from selected glass sections for micro-FTIR analyses in order to quantify the H_2O^{tot} and CO_2^{tot} contents within the glass. Mid- and Near-IR spectra (between 1000 and 6000 cm^{-1}) were obtained for 100x100 μm spot size using a Continuμm$^{©}$ microscope attached to a Nicolet$^{©}$ 5700 Fourier transform infrared spectrometer. A KBr beamsplitter and MCT-B detector were used to collect 128 scans (for sample and background) at a resolution of 4 cm^{-1}. The atmospheric contribution (in particular water) was reduced by enclosing the sample in a box purged with dry air during at least 20 minutes before analysis. Prior to sample acquisition, an instrumental background was taken to subtract the atmospheric contribution.

Several spectra (>3) are taken on different locations in the glass plate and results show that H_2O-CO_2 are evenly distributed across the sample. A volatile-free FTIR spectrum was taken on a dry glass synthesized at 1400°C, 1 atm. and was subtracted from each

volatile-bearing samples spectrum. Thickness measurements are done with a Mitutoyo[©]

digitometer with an accuracy of 1 μm. All spectra are then normalized to 100 μm for

quantitative analysis.

2.4. ^{13}C-MAS NMR:

Solid State ^{13}C-MAS NMR experiments of the partially crushed samples were acquired

on a 500 MHz Bruker Avance ($B_0 = 11.7$ T). A 4 mm Triple channel CP/MAS "Double

Bearing" probe was employed and the samples loaded in a ZrO_2 rotor with Teflon end-

cap. Rotors were spun at 10 kHz. The measurements were made at the [13]C Larmor

frequency (125.75 MHz). All spectra are referenced against TMS (Tetramethylsilane).

Table 2 gives the NMR analytical conditions which we used to analyse our glass samples.

For all samples, ^{13}C-MAS NMR spectra were acquired with single $\pi/4$ excitation of 2 μs

(SPE spectra). For several samples, ^{13}C-MAS NMR spectra were also acquired by using a

rotor-synchronised spin-echo sequence ($\pi/2 - \tau - \pi - \tau - acq.$) with a $\pi/2$ pulse of 4 μs

and τ equal to one rotor period. The second pulse rephases the spin system (Hahn, 1950)

due to dephasing of the signal because of external heterogeneity in the magnetic field and

dipolar interactions (Taylor, 2004; Xue and Kanzaki, 2004). Thus the loss of collected

signal due to the instrumental dead time is reduced. The rotor synchronised echo

sequence has also the advantage to suppress probe background signal (Zeng et al., 1999).

However, the probe signal does not perturb the ^{13}C signal acquisition as the concentration

in ^{13}C atoms in the probe is relatively low (rotor ZrO_2, stator: BN). These 2 kinds of

spectra will be referred hereafter as Direct MAS spectra (see Table 2).

[13]C-species can have long spin lattice relaxation time in silicate glasses (several minutes, Kohn et al., 1991). We tested several recycle time D1 (2 to 30 s) values to check for the consistency in the response of the C-species. No noticeable difference in term of line shape and chemical shift signatures was observed (only the peak absolute intensity will change) in the resulting spectra suggesting that all ^{13}C-species have similar spin-lattice relaxation behaviour. Similar observation was established by Maekawa et al. (1991) for the analysis of [29]Si which is recognized to possess a very long spin-lattice relaxation time. {^{1}H} ^{13}C-CPMAS NMR sequence was also employed to investigate ^{1}H and ^{13}C proximity and spatial relationship in the glass (Schmidt et al., 2000; Puls and Eckert, 2006). This method is selective but non quantitative. As mentioned in Robert et al. (2001), CPMAS involves 3 steps: 1) excitation of ^{1}H, 2) contact time (*ct*) and 3) acquisition of the ^{13}C spectrum. The radio-frequency conditions (the so-called Hartmann-Hahn conditions) applied during *ct* (a few ms) induce a through-space transfer of magnetization from the ^{1}H to the [13]C. The gain of sensitivity and signal is therefore a function of the time length and the dipolar coupling in between ^{1}H and [13]C. The transfer of magnetization is efficient from ^{1}H considered as an abundant nucleus compared to ^{13}C which is less abundant. Structural information can be obtained by comparing CP and non-CP spectra. Considering that the signal of ^{13}C environment in the proximity of ^{1}H will be enhanced, spatial structural information can be obtained on the [13]C-^{1}H relationship within the melt structure.

We applied several *ct* time length for investigating the magnetization transfer dynamic. As shown in Table 2, the *ct* time has been varied between 0.5 to 3.5 ms for two samples (7-1-*red* and 7-2). Dynamic CPMAS has proven very useful to probe the hydrogen

proximity to other nuclei (e.g. Xue and Kanzaki, 2004; Cody et al., 2005). At short ct (0.5 ms), only very close ^{1}H atoms to structural ^{13}C units will be enhanced by the transfer of magnetization whereas structural units with spatially far apart ^{1}H atoms will be decrease in intensity. At longer ct (3.5 ms), all ^{13}C structural units will undergo the influence of all ^{1}H atoms in their vicinity. During CPMAS experiment, the proton repetition time D1 = 2 s was sufficient for total relaxation before applying the next pulse sequence.

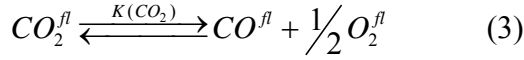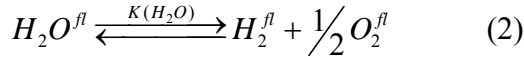^{1}H decoupling during acquisition (SPINAL64 scheme with a rf field of 60 kHz, Fung et al., 2000) was used to prevent from broadening of the ^{13}C lines due to heteronuclear interactions with protons (Laws et al., 2002).

We collected a large number of scans for obtaining a good S/N ratio with such a low ^{13}C abundances within the melt (~0.1 wt.% ^{13}CO$_2$ with ^{13}C/^{12}C = 0.8 at the best). Thus, depending on D1 values, between 2,000 and 36,000 scans have been co-added. The obtained free-induction-decay signal was treated with a low line broadening exponential function (50 Hz) preventing from loss of structural information (in particular for sharp peak signature) but decreasing the S/N ratio (6-1-ox is one typical example for low S/N ratio).

3. Methods for log fO$_2$ calculation:

Two methods were employed to determine the log fO$_2$ experienced by the samples: 1) from H$_2$O^{tot} dissolved in the melt and 2) from fluid inclusion composition in the system CO$_2$-CO. Both methods are fully described in Morizet et al. (2009) and the reader is redirected to that publication for thorough details. The calculation method is based on thermochemical equilibrium involving reactions for H$_2$O and CO$_2$ dissociation:

$$H_2O^{fl} \xrightleftharpoons{K(H_2O)} H_2^{fl} + \frac{1}{2}O_2^{fl} \qquad (2)$$

$$CO_2^{fl} \xrightleftharpoons{K(CO_2)} CO^{fl} + \frac{1}{2}O_2^{fl} \qquad (3)$$

for each reaction the equilibrium constant is defined as follow:

$$K(H_2O) = \frac{fH_2 \times fO_2^{\frac{1}{2}}}{fH_2O} \qquad (4)$$

$$K(CO_2) = \frac{fCO \times fO_2^{\frac{1}{2}}}{fCO_2} = \frac{X(CO)\phi(CO) \times fO_2^{\frac{1}{2}}}{X(CO_2)\phi(CO_2)} \qquad (5)$$

Where in Eq. (4) and (5), f_i is the fugacity, X_i is the molar fraction and Φ_i is the fugacity coefficient for the i fluid species.

Both methods require constraining the fluid phase composition. In Eq. 4, the fH_2 is determined from experimental conditions (see above); K(H$_2$O) is calculated using the thermodynamic modeling from Shi and Saxena (1992); and fH_2O in the fluid phase is derived from the model of Dixon et al. (1995) which relates the total H$_2$O dissolved within the glass to the H$_2$O fugacity in the fluid.

In Eq. 5, we used CORK equation from Holland and Powell (1991) to calculate the Φ, the fugacity coefficients of the different species. The K(CO$_2$) was calculated from the thermodynamic model of Shi and Saxena (1992). The molar fraction (X) of the fluid

16

species was determined from Micro-Raman analysis of the fluid inclusions and using the calibration curve from Morizet et al. (2009).

Results on the fluid phase composition are given in Table 1. The actual $X(CO_2)$ and $X(CO)$ values measured by micro-Raman are calculated taking into account the presence of H_2O within the fluid phase and according to Eq. (6):

$$X(H_2O) + X(CO_2) + X(CO) = 1 \qquad (6)$$

In this equation, the $X(H_2)$ is neglected as under the moderately investigated reducing conditions, this species will not be present in significant quantity. Values for $X(H_2O)$ were obtained from the thermodynamic equilibrium of Eq. (7):

$$X(H_2O) = \frac{f(H_2O)}{P_{tot} \cdot \phi(H_2O)} \qquad (7)$$

As can be seen from Table 1, the $X(H_2O)$ makes up a considerable part of the fluid inclusion composition and has been included into the thermodynamic calculation in Eq. 5.

The log fO_2 determined from the two methods (either fluid inclusion analysis or H_2O dissolved in the melt) compare well to each other as shown in Table 1 and Figure 1. In Figure 1, the log fO_2 (1) represents the value determined from H_2O^{tot} dissolved in the melt and the log fO_2 (2) is the value determined from the $X(CO_2)$-$X(CO)$ in the fluid inclusions. We observe a good agreement between the two approaches. The error on the

log fO_2 was calculated considering 1) an upper and lower value for $X(CO_2)$-$X(CO)$ for

fluid inclusions analyses and 2) an upper and lower value for H_2O^{tot} dissolved in the glass

(see Table 3). The log fO_2 (2) value shows the least variation consistent with the small

variation of fluid inclusions compositions. The maximum error for log fO_2 (2) is for 3-1

with -8.03 ±0.24. The log fO_2 (1) variation is slightly higher with a maximum error for 7-

1-red with -10.29 ±0.38.

For the remaining of the paper and because we do not consider one value more

representative than the other, we will refer to an intermediate value between log fO_2 (1)

and (2). Values relative to ΔFMQ will be used. Calculations relative to solid buffer were

accomplished with the model of Zolotov and Fegley (1999) and with the thermodynamic

dataset from Robie and Hemingway (1995).

Log fO_2 values experienced in our study cover a range from oxidized for 6-1-*ox* at

ΔFMQ+2.6 to reduced conditions for 7-1-*red* at ΔFMQ-2.6. Those values can be directly

applied to modern Earth interior degassing (e.g. Kadik et al., 2004; Behrens and Gaillard,

2006) but also to Mars interior degassing (Hirschmann and Withers, 2008).

4. Results:

4.1 Micro-Raman spectral feature:

4.1.1. Fluid inclusion analysis:

From Micro-Raman analyses, we identified 3 main species present within the fluid

inclusions: CO_2^{fl}, CO^{fl} and CH_4^{fl} (H_2O^{fl} is also present but not quantified by Micro-

Raman). Micro-Raman spectra obtained from fluid inclusions and for 4 different samples

are shown in Figure 2. The Raman shift is separated in several windows showing the

gaseous vibrational signature of interest: Figure 2A for CO_2^{fl}; Figure 2B for CO^{fl} and Figure 2C for CH_4^{fl}. We applied an intensity scaling factor of 2 in Figure 2B and 4 in Figure 2C in order to increase the size of the CO peaks and CH_4 peaks. The CO_2 vibration consists in 2 modes: $2\nu_2$ and ν_1; those signatures are located at ~1385, 1285 cm$^-$ ^{1} for $^{12}CO_2$ and ~1370, 1260 cm^{-1} for $^{13}CO_2$. The CO vibration has only 1 mode located at 2138 cm^{-1} for ^{12}CO and 2093 cm^{-1} for ^{13}CO. A small quantity of CH_4 has been identified in the most reduced samples and is shown in Figure 2C with a signature at 2909 cm^{-1} for $^{12}CH_4$ and 2914 cm^{-1} for $^{13}CH_4$.

From the fluid inclusion analysis, we can see that in most of the cases both ^{12}C and ^{13}C isotopes are present (except for 2-2-^{12}C ΔFMQ-2.0 which is a ^{12}C natural sample). This is consistent with the incomplete decarbonation of the starting material. We have calculated the ^{13}C enrichment following the method Morizet et al. (2009). The values for the %^{13}C within the fluid are reported alongside the spectra in Figure 2A and for all studied samples in Table 1.

The method to determine the concentration of each species in the fluid inclusions is fully described in Morizet et al. (2009). The area of each peak is directly proportional to the concentration of the species. For CO_2 the best calibration was obtained when the $2\nu_2$ mode was considered. We only use this mode in the $X(CO_2)$ calculation reported in Table 1 and Figure 2B. The error on the measured molar fraction was calculated from standard deviation based on replicated analyses on different fluid inclusions (>3) within each sample. The maximum error is observed for 4-1 with $X(CO_2) = 0.628 \pm 0.049$ which is less than 10%. The reported error is consistent with error given in Morizet et al. (2009) and suggests that fluid inclusions are well-equilibrated across the sample showing little

variation in composition. The $X(CO_2)$ values shown in Figure 2B are the corrected values

which take into account the presence of H_2O within the fluid inclusions (see Table 1).

Thus, $X(CO_2)$ is roughly constant (~0.52) for 7-2 (ΔFMQ-1.2), 2-2-^{12}C (ΔFMQ-2.0) and

7-1-*red* (ΔFMQ-2.6) but the $X(CO)$ is increasing progressively from 0.11 to 0.41 as

shown in Table 1 accompanying a decrease in fO_2 conditions from ΔFMQ-1.2 to -2.6.

A peak at 2900 cm^{-1} and corresponding to CH_4 is observed in the most reduced sample at

ΔFMQ-2.0 and ΔFMQ-2.6 and is totally absent for the most oxidised samples. CH_4 only

corresponds to a few percent compared to the other species. We choose to compare CH_4

and CO to derive the $\%CH_4$ as follow:

$$\frac{\%CH_4}{\%CO} = \frac{A_{CH_4}}{\zeta\sigma_{CH_4}} \times \frac{\zeta\sigma_{CO}}{A_{CO}} \qquad (8)$$

In Eq. (8), A is the area of the peak species, σ is the cross-section factor for the species

and ζ is the efficiency factor which is defined for a given spectrometer. We have

quantified the $\%CH_4$ reported in Figure 2C using 7.5 as the cross-section calibration

factor (Burke, 2001). The ratio $\sigma CH_4/\sigma CO$ between the cross-section factors is roughly

~8, hence for similar CH_4 and CO peak area the concentration of CH_4 will be 8 times

lower than CO. The resulting $\%CH_4$ is small. In the most reduced sample 7-1-*red*, the

$\%CH_4$ estimated is 3% and thus the molar fraction of CH_4 within the fluid phase is

roughly 0.03 at best. The CH_4 can be related to other species by the following

equilibrium:

$$CO_2^{fl} + 2H_2^{fl} \xrightleftharpoons{K(CH_4)} CH_4^{fl} + O_2^{fl} \quad (9)$$
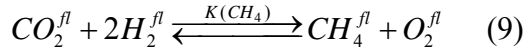
We calculated the fO_2 from this reaction and for the most reduced sample in which the CH$_4$ concentration is the most significant. The equilibrium constant for reaction (9) reads as follow:

$$K(CH_4) = \frac{fCH_4 \times fO_2}{fCO_2 \times P(H_2)^2} = \frac{X(CH_4)\phi(CH_4) \times fO_2}{X(CO_2)\phi(CO_2) \times P(H_2)^2} \quad (10)$$

Using K(CH$_4$) from the thermodynamic model of Shi and Saxena (1992), Φ from the CORK equation of Holland and Powell (1991), P(H$_2$) from the experimental conditions (7-1-*red* is equal to 68 bars), and X(CO$_2$) = 0.53, give an fO_2 equal to ΔFMQ-3.8. This is considerably lower than the values calculated from the two other methods (ΔFMQ-2.6, Table 1). To increase the fO_2, would require to decrease the concentration of CH$_4$. For instance a calculation done with X(CH$_4$) = 0.004 (7-2 sample) gives an fO_2 of ΔFMQ-2.9 compared to ΔFMQ-1.2 reported in Table 1 and calculated from the other methods. Another source of error comes from the experimental P(H$_2$) which may be slightly different from the one given in Table 1. Anyhow, it appears that the observed CH$_4$ in fluid inclusions is difficult to quantify and therefore is not suitable for fO_2 calculation.

4.1.2. H_2O^{tot} quantification:

We tested the possibility to determine the H_2O^{tot} through Raman acquisition and following the method described by Behrens et al. (2006). We show in Figure 3 the Micro-

Raman spectra of different glasses between 200-1250 cm^{-1} and 2700-3900 cm^{-1}. Several vibrational signatures are observed within each spectrum. The broad asymmetric peak with maximum at 3500 cm^{-1} is attributed to OH stretching (e.g. Ihinger et al., 1994; Thomas, 2000; Zajacz et al., 2005; Mercier et al., 2009). Two pronounced signatures are observed for the glass structure. Bands at 500 and 1000 cm^{-1} are assigned to T-O-T bending and rocking and T-O stretching respectively (Frantz and Mysen, 1995; Behrens et al., 2006). The 1000 cm^{-1} high intensity is consistent with basaltic composition as mentioned by Behrens et al. (2006). More silicic composition will show a more intense vibrational signature at 500 cm^{-1} compared to T-O stretching at 1000 cm^{-1}.

A typical non-linear baseline is represented underneath the spectra and was used to derive the peak area for integration. The baseline is arbitrary however it mimics the continuum of the Raman spectra adequately. Moreover, the good agreement with the FTIR quantification (see Figure 9 and Table 3) suggests that our approach is satisfactory. Spectra shown here are not corrected for black-body radiation (Long, 2002). The correction procedure does not seem to improve the baseline in the case of our composition, although it tends to complicate the positioning of the non-linear baseline for water quantification. The water content derived from this method (H_2O^{tot} (2)) is given next to each spectrum and in Table 3 for all samples. The results obtained using both methods FTIR and Micro-Raman will be further discussed later in section 4.4.

4.2 FTIR spectral features:

4.2.1. Carbonate environment:

22

Carbonate species (CO_3^{2-}) are represented in Figure 4 by a complex "doublet" assigned to the carbonate antisymmetric stretch (v_3) located between 1300 and 1600 cm^{-1} consistent with the description given by Fine and Stolper (1986). Only carbonate units are present in our haplobasaltic composition. No evidence of CO_2^{mol} at 2350 cm^{-1} (Brooker et al., 1999; Behrens et al., 2004) has been identified and also consistent with NMR results. This observation is in agreement with currently known CO_2 dissolution mechanisms: CO_2 speciation changes from CO_2^{mol} towards CO_3^{2-} units progressively from rhyolitic to basaltic composition (Blank and Brooker, 1994; King and Holloway, 2002; Behrens et al., 2004). However, it should be mentioned that the speciation observed is the CO_2 speciation preserved at the glass transition temperature (Tg) as demonstrated by recent work (e.g. Morizet et al., 2001; Nowak et al., 2003; Spickenbom et al., 2010). Therefore, the measured CO_2 speciation does not represent the true CO_2 speciation present in the melting conditions at which CO_2^{mol} is expected.

No vibrationnal mode for C-O stretching is seen around 2150 cm^{-1} which would have attested for the presence of CO^{mol} (Brooker et al., 1999). The absence of CO^{mol} is consistent with previous findings from Pawley et al. (1992) who suggested that the CO^{mol} species is not soluble in basaltic glass at least under its molecular form. However, it is not excluded that CO^{mol} would be present under those reduced conditions at high temperature within the melt consistent with C speciation behaviour above Tg. The signature visible at 1630 cm^{-1} is attributed to water vibration and corresponds to total H_2O bending mode (Ihinger et al., 1994).

We have stated that due to incomplete decarbonation the synthesized glasses have different ^{13}C enrichment. We show the FTIR spectra for ~80%, 40% and 1% [13]C

enrichment within the fluid phase in Figure 4A, B and C, respectively. In all cases, the carbonate peak maxima are shifted progressively to higher frequency when the $\%^{13}C$ decreases. In Figure 4A (80% ^{13}C in fluid) the peak maxima are located at ~1404 and ~1482 cm^{-1} giving a centre point at 1443 cm^{-1} and a $\Delta v_3 = 78$ cm^{-1}. In Figure 4C (1% ^{13}C in fluid) the peak maxima are displaced at ~1438 and 1520 cm^{-1} with a centre point at 1479 cm^{-1} and $\Delta v_3 = 82$ cm^{-1}. The shift in peak position is consistent with the change in isotopic enrichment in ^{13}C. According to Hooke's law, it is possible to predict the peak position (v in cm^{-1}) of a vibration as a function of the reduced mass (Ihinger et al., 1994). The v value is inversely proportional to the square root of the reduced mass of the atoms implied into the vibration. As such, a vibration involving a ^{13}C atom will have a lower frequency position compared to the same vibration with a ^{12}C atom involved which is in agreement with the results shown in Figure 4. We estimated the change in reduced mass between ^{12}C and ^{13}C for a C-O vibration. We obtain a scaling factor ($^{13}C/^{12}C$ v(C-O)) of 1.0460 and its square root 1.0227. The value of 1.0227 is directly correlated to the frequency shift between the two isotopes. It is in excellent agreement with the change in peak position between ^{13}C-enriched and -poor samples observed in Figure 4: 1438 / 1404 ~ 1.0242; 1520 / 1482 ~ 1.0256.

For a given enrichment, the peak maximum does not change as reduction of the samples proceeds as indicated by the dashed lines in Figure 4. Similarly, the Δv_3 remains constant and oscillates between ~65 and 82 cm^{-1} for 40% and 1% ^{13}C respectively. The lowest Δv_3 value for 40% ^{13}C reflects the fact that those samples are a mixture of both ^{12}C-^{13}C isotopes and therefore the peak positions are intermediate in between the one observed for ^{13}C-poor glasses (Figure 4C, 1% ^{13}C) and ^{13}C-rich glasses (Figure 4A, 80% ^{13}C). The

very small value for Δv_3 suggests a low distortion from the ideal trigonal planar symmetry (D_{3h}) (Brooker et al., 2001b). Such a value is often observed for natural basaltic or similar compositions (Fine and Stolper, 1986; Taylor, 1990).

4.2.2. Water band assignment:

Infrared spectra in Figure 5A show that H_2O dissolves in the melt as two main species: i) hydroxyl unit (OH^-) and ii) molecular water (H_2O^{mol}). The peak located at 4500 cm^{-1} is attributed to OH groups and peak at 5200 cm^{-1} is assigned to H_2O^{mol} as suggested by previous studies (e.g. Stolper, 1982a; King et al., 2002; Stuke et al., 2006). An additional signature is given by the fundamental OH stretching vibration band at 3500 cm^{-1} and represented for several spectra in Figure 5B (except for sample 7-2 for which no spectrum was resolved in this frequency range due to the high water content saturating the FTIR detector). For the clarity of Figure 5 we did not represent the whole set of glass spectra as it turn out to present the same line shape for all and only differs in the H_2O^{tot} measured within the glass.

We fitted a baseline (dashed line) to mimic the background for the FTIR continuum underneath the OH and H_2O^{mol} peaks in Figure 5A and the peak for H_2O^{tot} in Figure 5B. In most cases, this procedure is easily performed and the integration of the peaks for quantification is straightforward. This is true in particular for the peak at 3500 cm^{-1} for which a tangential linear baseline has been fitted as shown for 6-1-*ox*, 4-1 and 7-1-*red*. The quantification of each individual species (OH and H_2O^{mol} peaks) is sometime complicated by the presence of interference lines which are due to the low thickness (<60 μm) of the glass doubly polished plate.

The different concentrations (OH, H_2O^{mol} and H_2O^{tot}) as well as the ΔFMQ value are indicated in Figure 5 and listed in Table 3. At low water content (< 2 wt.% H_2O^{tot}), the water speciation is mainly represented by the OH groups at 4500 cm^{-1}. With further increase in H_2O^{tot} as for 6-1-*ox* and 7-2, there is a progressive increase in the peak intensity for H_2O^{mol} vibration. This behavior is in agreement with known H_2O speciation trends showing a crossover between the two species at ~4 wt.% H_2O^{tot} (e.g. Dixon et al., 1995; Withers and Behrens, 1999; Botcharnikov et al., 2006).

4.3 ^{13}C-MAS NMR:

4.3.1. Carbonates environments from Direct ^{13}C MAS NMR:

^{13}C MAS NMR spectra for several samples (with increasing log fO_2) are represented in Figure 6. The log fO_2 relative to ΔFMQ and the ppm CO_2 is also indicated next to each spectrum.

Several species are identified from NMR spectra. $^{13}CO_2$ and ^{13}CO in fluid are observed and are located 125 and 183.5 ppm respectively (Kohn et al., 1991; Morizet et al., 2009). Those species are entrapped within fluid inclusions. The sharp peaks are consistent with free motion for "gaseous" molecules and therefore cannot be attributed to dissolved species within the glass. When present, fluid inclusions are mainly constituted by $^{13}CO_2$ and, for the most reduced sample, by additional ^{13}CO. No signature for $^{13}CH_4$ at 0 ppm (Ripmeester and Ratcliffe, 1988; Subramanian et al., 2000) is seen in the different spectra which is consistent with the low concentration of CH_4 measured by Micro-Raman analysis (< 3% CH_4).

Dissolved C species are represented by carbonate units with signature located at chemical shift between ~160 and 170 ppm. The peak does not show a significant asymmetric shape and has its maximum at ~167 ppm regardless of the redox conditions.

There is no evidence for other species than carbonates to be dissolved within the glass. NMR results are consistent with the FTIR measurements showing only the carbonate peak doublet. The ^{13}C NMR spectra do not reveal the presence of more reduced species such as CH_3 at ~15 ppm (Khimyak and Klinowski, 2001). Mysen et al. (2009) suggested the presence of methyl groups dissolved within Na_2O-SiO_2 glasses synthesized under high pressure (1.0-2.5 GPa) and highly reducing conditions (IW buffer). The formation of CH_3 groups thus seems to be restricted to severe reducing conditions and is not possible under our moderate reducing conditions.

Several samples with different redox conditions were analyzed. In Figure 6 ^{13}C MAS NMR spectra for oxidized (ΔFMQ+2.6) and reduced (ΔFMQ-0.1 to -2.6) glasses are almost identical in lineshape. It appears there is a slight broadening of the 6-1-*ox* peak line shape which is attributed to the high concentration of paramagnetic impurities (1.17 wt.% FeO^{tot}). NMR and FTIR spectra give consistent results as no dramatic change is observed in the carbonate environments as a function of fO_2.

^{13}C NMR spectra obtained for haplophonolite (Morizet et al., 2002) and sodamelilite (Kohn et al., 1991) have been added for comparison with our haplobasaltic glass samples. Both spectra have a better S/N ratio compared to our glass spectra. The phonolite and sodamelilite glasses from Morizet et al. (2002) and Kohn et al. (1991) were synthesized at high pressure, 2.0 and 1.0 GPa respectively and under moderately oxidizing conditions; hence the total CO_2 solubility is very high (several wt.%).

Our ^{13}C-NMR spectra for haplobasaltic glasses is similar to haplophonolite spectrum from Morizet et al. (2002). The peak maximum is identical at 167 ppm; the full width at half maximum (FWHM) is almost equal with 7 and 8 ppm for the basalt and phonolite respectively. One major difference is the clear asymmetric shape observed in haplophonolite glass at lower frequency suggesting the existence of several carbonate units.

Our haplobasaltic glass is different from sodamelilite glass spectrum obtained by Kohn et al. (1991). For sodamelilite, the peak maximum is slightly shifted to higher frequency at 168 ppm, the peak is symmetrical (one unique carbonate environment) but has a lower FWHM of ~4.5 ppm.

For haplobasaltic glass, the poor S/N ratio renders difficult the interpretation of the spectra. However, the results obtained by $\{^1H\}$ ^{13}C CPMAS experiments will comfort the existence of several carbonate groups within our haplo-basaltic glasses.

4.3.2. Carbon and hydrogen proximity revealed from $\{^1H\}$ ^{13}C CPMAS NMR:

We performed $\{^1H\}$ ^{13}C CPMAS to investigate the possibility for the carbonate environments to be spatially close to hydrogen atoms. $\{^1H\}$ ^{13}C-CPMAS NMR spectra (ct = 3.5 ms) are shown in Figure 7 for 5 different samples (see Table 2).

In Figure 7 the ΔFMQ and the H_2O^{tot} are indicated for the different samples. Unfortunately, we did not obtain a reliable signal from the most oxidized sample, 6-1-*ox* (ΔFMQ+2.6) possibly due to the high FeO^{tot} of this sample.

The line shape of the spectra is varying in between the samples. A peak at 167 ppm is observed for all samples consistent with ^{13}C Direct MAS NMR spectra (see Figure 8). A second component is appearing in, 4-1 and 7-1-*red* and possibly 7-2 at 177 ppm. This component is invisible in Direct MAS spectra as shown in Figure 8. The corresponding carbonate group is probably below the detection limit and can only be observed when the ^{13}C signal is enhanced by the transfer of magnetization from neighboring hydrogen atoms. The other carbonate group is always present and contributes to the majority of the carbonate environments within the glass. Although the concentration of the 177 ppm component is low, it cannot be ignored and is clearly implied in the reduction process of the basaltic liquid during the experiment.

The 177 ppm component is not correlated to the H_2O^{tot} as observed from the spectra reported in Figure 7. On the other hand, we can see that its appearance or intensity for a given contact time in 4-1 and 7-1-*red* seems to be directly correlated to the degree of reduction experienced by the samples. When reduction is maximum (at high fH_2), the additional component is revealed in 4-1 and even more in 7-1-*red* by CPMAS.

The advantage of {^{1}H} ^{13}C CPMAS is to provide indication on the ^{1}H environment of the different ^{13}C units. The fact that 177 ppm appears in CPMAS whereas it is totally absent in Direct MAS suggests that this carbonate unit possesses a higher hydrogenated (higher OH concentrations) environment than the carbonate groups at 167 ppm.

We made the comparison in Figure 8 between ^{13}C Direct MAS and {^{1}H} ^{13}C CPMAS spectra acquired with different $ct = 0.5$, 1.0 and 3.5 ms. The spectra are plotted normalized to the same number of scans (8,192) so one can easily compare the change in intensity of the different unit depending on ct. The dynamic {^{1}H} ^{13}C CPMAS reveals

that the carbonate group at 177 ppm is preserved and increases as the *ct* is decreased from

3.5 to 0.5 ms. Conversely, the peak at 167 ppm decreases in intensity as the *ct* is

decreased from 3.5 to 0.5 ms. This result implies that hydrogen atoms in the 177 ppm

carbonate group are spatially closer than for the 167 ppm carbonate environment. We can

also see that the 177 ppm component has a maximum intensity at 0.5 ms in the case of 7-

2 suggesting a strong dipolar coupling between hydrogen atoms which could be

explained by the higher water content (3.66 wt.% H_2O).

4.4 CO_2 and H_2O concentrations measured in glasses:

H_2O and CO_2 quantifications from FTIR were achieved using Beer-Lambert law (e.g.

Ihinger et al., 1994; King et al., 2002; Morizet et al., 2002; Okomura et al., 2003).

$$C_i = \frac{Abs_i \cdot MM_i}{\rho \cdot d \cdot \varepsilon_i} \qquad (11)$$

where C_i, the concentration of i-species, is a function of the integrated absorbance of the

peak vibration (Abs_i) times the molecular mass (MM_i, 18.02 and 44.01 $g.mol^{-1}$ for H_2O

and CO_2 respectively) and divided by the product between the density (ρ, $g.L^{-1}$), the

thickness of the sample (d, cm) and the integrated molar extinction coefficient for the

considered specie (ε_i, $L.mol^{-1}.cm^{-2}$). A density value of 2537 $g.L^{-1}$ was used and

determined from the Lange and Carmichael (1987) density model. This density value

does not take into account the potential effect of H_2O on the glass density (Ohlhorst et al.,

2001), however in the range of water content studied here (up to 4 wt.% H_2O) the expected change in density is roughly ~2.5% of the value and therefore will be neglected.

4.4.1. H_2O concentration determined from Micro-FTIR and Micro-Raman:

The H_2O^{tot} was determined using either the H_2O^{tot} peak at 3500 cm^{-1} (for most of the samples) or the sum of the OH + H_2O^{mol} contribution at 4500 and 5200 cm^{-1} respectively (see Table 3). FTIR quantification can only be achieved if suitable values for ε are available; however those values are depending on glass composition (Ohlhorst et al., 2002; Mandeville et al., 2002).

For OH and H_2O^{mol}, we used an ε value derived by Stolper (1982) and valid for a basaltic composition: 200 L.mol^{-1}.cm^{-2} for OH groups and 300 L.mol^{-1}.cm^{-2} for H_2O^{mol}. We summed both concentrations of OH and H_2O^{mol} to determine the total water content, H_2O^{tot} (1). The error reported in Table 3 for OH and H_2O^{mol} is obtained from the standard deviation analysis and the error on H_2O^{tot} (1) is then calculated. The maximum error for the H_2O^{tot} (1) observed is ±0.30 wt.% H_2O for 6-1-*ox* sample.

For the total water content with the peak located at 3500 cm^{-1} (H_2O^{tot} (3500 cm^{-1}), see Table 3), we tested several extinction coefficient values. H_2O^{tot} (3500 cm^{-1}) was calculated using either linear or integrated extinction coefficient. The associated error was derived from standard deviation analysis. Using the integrated (32000 L.mol^{-1}.cm^{-2}) or linear value (67 L.mol^{-1}.cm^{-1}) given by Stolper et al. (1982) gives results in relatively good agreement with the results obtained from H_2O^{tot} (1) as the sum of OH + H_2O^{mol}. However with high water content, the agreement between the two determined values disappears (see Figure 9). It is particularly true for 7-2 and 3-1 samples for which we

31

obtained a high water content from H_2O^{tot} (1) (> 3 wt.%) and a totally different value for

H_2O^{tot} (3500 cm^{-1}). The obvious lack of consistency for those two samples can be

explained by the fact that at high water content, the quantification with the peak at 3500

cm^{-1} becomes uncertain. The 3500 cm^{-1} peak cannot be resolved and the intensity turned

out to be too high and saturates the IR detector leading to wrong H_2O^{tot} (3500 cm^{-1})

value. As such, we could not determine the water content with this method for sample 5-1

due to incomplete resolution of the FTIR peak at 3500 cm^{-1}.

Mandeville et al. (2002) recently investigated the change in the extinction coefficient

value as a function of the glass composition and for the peak at 3500 cm^{-1} for water

quantification. In particular, they derived a value of 69.21 L.mol^{-1}.cm^{-1} calibrated for an

Fe-free andesite composition. This value is very close to the one derived by Stolper et al.

(1982). In a more general point of view, the change in the extinction coefficient

especially for the peak at 3500 cm^{-1} is relatively small (Mandeville et al., 2002) for the

type of glass composition investigated here and the impact on the H_2O^{tot} variation is

negligible as shown in Figure 9. As a result, we are confident when using the ε values

proposed by Stolper et al. (1982) to determine the H_2O^{tot} (1) from the sum of OH and

H_2O^{mol} concentrations.

The H_2O^{tot} was also estimated using micro-Raman measurements (H_2O^{tot} (2) column in

Table 3) and following the method developed by Behrens et al. (2006). The procedure

has been successfully applied by those authors for various compositions (ranging from

granite to basalt) and a large range of water content (from 0.5 to 11 wt.% H_2O^{tot}).

Although the method is proposed to be suitable only for one type of spectrometer

(T64000 Jobin Yvon), we show that the obtained results with our equipment (LabRam

Jobin Yvon) are in good agreement with the FTIR results suggesting that the method can also be applied for LabRam spectrometer.

The integrated area of water broad vibrational frequency at 3500 cm^{-1} is normalized to the aluminosilicate vibration mode at 1000 cm^{-1} (see Figure 3). The H_2O^{tot} is then obtained directly using the linear regression proposed for basaltic composition by Behrens et al. (2006, their Eq. 3). As shown in Table 3 and Figure 9, results obtained from both methods FTIR and micro-Raman are in good agreement. A typical error of ±0.20 as given in Behrens et al. (2006) was taken.

The final retained value for H_2O^{tot} is given in the last column in Table 3 and represents an intermediate value between the H_2O^{tot} (1) and H_2O^{tot} (2) and ranges from 1.24 to 4.01 wt.% H_2O. The error associated with the values is estimated to be ±0.20 which is i) the average error observed for H_2O^{tot} (1) and ii) the assumed error value for H_2O^{tot} (2). Though, this error value is rather typical when estimating volatile concentrations from spectroscopic method.

4.4.2. CO_2 concentration determined from Micro-FTIR:

Carbonate doublet were integrated for CO_2 quantification. The procedure is different as compared to water quantification as there is complication due to the presence of the strong vibrational signature for ν_2 H_2O at 1630 cm^{-1}. Subsequently, we used a simulation of the spectrum with 3 Gaussian peaks: 1) 1630, 2) 1430 and 3) 1530 cm^{-1}. We fitted and subtracted a flexicurve baseline prior to the simulation. This approach is suitable for basalt-like compositions (e.g. Silver et al., 1990; Zhang et al., 1995; Olhorst et al., 2001). We used the sum for both CO_3^{2-} peaks to obtain the absolute integrated area of the

carbonate doublet. The main advantage of the simulation method is to remove the possible contribution of the ν_2 H_2O tail at 1630 cm^{-1} to the carbonate doublet. The simulation of the spectrum is not represented, yet the procedure is relatively robust with a correlation factor $R^2 \sim 0.98$. We applied the Beer-Lambert approximation with a value for ε of 69500 L.mol^{-1}.cm^{-2} as determined by Fine and Stolper (1986) for natural basaltic and Ca-Mg silicate glasses. The total CO_2 content is given in Table 3 and ranges from 223 to 1320 ppm.

There is a clear lack of appropriate extinction coefficient data which are known to be a strong function of composition (Ihinger et al., 1994). Our studied composition is not identical to that of Fine and Stolper (1986) and the $\varepsilon(CO_3^{2-})$ for our haplobasaltic glass is expected to be slightly different from this value of 69500 L.mol^{-1}.cm^{-2}. Moreover, it has been applied for ^{12}C carbonate groups and may not be valid for ^{13}C isotopes carbonate band. However, there is up to now no calibration available for $^{13}CO_2$-bearing glasses investigated by FTIR.

4.4.3. CO_2 versus H_2O concentrations

The CO_2^{tot} versus H_2O^{tot} dissolved in the quenched glasses is shown in Figure 10. As mentioned above, CO_2 ranges from 223 ppm for 4-2-*us* (initially CO_2-free sample) to 1320 ppm for 6-1-*ox*. H_2O^{tot} is changing from ~1.24 wt.% for 1-1-*200* to 4.01 wt.% for 5-1. 1-1-*200* has a lower CO_2 content because it was synthesized at lower pressure. 4-2-*us* was initially a CO_2-free sample but because of incomplete decarbonation we measured a non negligible amount of CO_2, 223 ppm.

Other samples were synthesized at 300 MPa total pressure and at temperature of 1250°C.

Apart from the 2 particular samples mentioned above, the H_2O^{tot} dissolved in the melt

(corresponding to the sum of the H_2O initially loaded in the capsule and the H_2O formed

from the H_2 diffusion inside the capsule) is relatively large ranging from ~1.3 up to 4.0

wt.%, for 3-2-^{12}C and 5-1 respectively. The change in H_2O^{tot} dissolved in the glass will

influence Tg position (Dingwell et al., 1998). Between 1 and 4 wt.% H_2O, the expected

decrease in Tg could be up to 100°C according to the model of Giordano et al. (2008).

The influence of different Tg values in the present study is difficult to apprehend

however it is possible that the C and H speciation could be affected by such changes.

In Figure 10, we distinguish 2 groups of data points: 1) one corresponding to severe

reducing conditions at roughly $\Delta FMQ < -1.5$ and 2) one to more oxidized conditions at

roughly $\Delta FMQ > -1.2$. One important difference noticed between the 2 groups is the

water content. The first group with strongly reducing conditions has lower H_2O content

whereas the second is constituted by 3 points with at least 3 wt.% H_2O. Although the

reason for those to be particular is unclear, Behrens et al. (2009) suggested that high H_2O

content could produce an increase in CO_2 solubility.

At 300 MPa, the CO_2 solubility data show a maximum at 1320 ppm for 6-1-*ox* and 681

ppm for 7-1-*red*. All data points are located within those 2 values. CO_2 solubility data

measured for reduced samples are systematically lower than the CO_2 solubility measured

for oxidized conditions for 6-1-*ox*. The change in CO_2 solubility is likely to be related to

the changes in fluid phase composition in response to fO_2 decrease (e.g., Pawley et al.,

1992).

Isobaric CO_2-H_2O solubility trends derived from Dixon et al. (1995) thermochemical equilibrium model at total pressure of 150, 200, 250 and 300 MPa have been represented by solid lines in Figure 10 and will be discussed in section 5.2.

5. Discussion:

5.1 Carbonate environments assignment:

We have attempted to simulate the spectra for the carbonate environments with several Gaussian peaks for 7-1-*red* and 7-2 shown in Figure 8. The simulation was performed with 2 peaks considering that 1) the main component at 167 ppm is symmetric in shape and can be the result of only one type of carbonate unit and 2) the presence of the additional peak at 177 ppm.

The respective positions for the 2 Gaussian peaks are 167 and 176.5 ppm. The full width at half maximum (FWHM) is ~7.5 ppm for the component at 167 and ~9.3 ppm for the peak at 176.5 ppm. The assignment for both CO_3^{2-} components is complicated by 1) the complex character of the studied composition (5 oxides), 2) the fact that the S/N ratio is often poor and 3) the little information available in the literature.

Infrared spectra suggest that the carbonate environments observed in the haplobasaltic glasses have a low distortion or, in other words, are very symmetrical molecules. This assertion is based on the small value for Δv_3 (< 80 cm^{-1}). Therefore, it is unlikely that such low Δv_3 would correspond to a so-called network carbonate. According to Brooker et al. (2001b), network carbonates such as T-carb.-T (with T = Si or Al) exhibit a large Δv_3 (> 200 cm^{-1}) inconsistent with our results. Moreover such network unit has been

mainly identified in fully polymerized melts which is not the case for the studied

haplobasaltic composition in which a non negligible amount of NBO is expected.

Following the work of Brooker et al. (2001b), such a low Δv_3 at 80 cm^{-1} could be

attributed to the presence of NBO-carb. Ca^{2+}. This assignment is also concordant with the

fact that i) NBOs should exist in our composition (NBO/T = 0.42), ii) the composition is

Ca-rich and Ca^{2+} is one important charge balancing cation and iii) the CO_2 solubility is

suspected to be in large part controlled by the Ca amount within the melt but less

influenced by Na and even less by Mg (Dixon, 1997). This point is also supported by

recent experimental work by Iacono-Marziano et al. (2008) showing a dramatic CO_2

solubility increase with increasing Ca^{2+} content.

We have a small amount of Na present in our glass (3.2 wt.% Na_2O) and thus the infrared

peak responsible for this can be perfectly hidden underneath the main infrared doublet

since NBO-carb. Na^+ has a lower distortion with Δv_3 ~35-45 cm^{-1}. Nevertheless, the

isotropic chemical shift for Na_2CO_3 is 171 ppm according to Jones et al. (2005). Thus, it

is unlikely that NBO-carb. Na^+ unit exists on the basis of the NMR results. However, it

should be mentioned that hydrated crystalline carbonate have lower chemical shift than

dry carbonates. For example, Nebel et al. (2008) showed that the ^{13}C NMR for $NaHCO_3$

is observed at 164 ppm.

In the light of infrared observations, we propose to assign the main NMR resonance at

167 ppm to NBO-carb. Ca^{2+}. Morizet et al. (2002) suggested a similar assignment for an

individual NMR component simulated at 168 ppm in haplo-phonolite glasses.

Our assignment of 167 ppm resonance to NBO-carb. Ca^{2+} is also consistent with recent

investigation on the structure of amorphous and crystalline calcium carbonates by Nebel

37

et al. (2008) and using ^{13}C Solid-State NMR spectroscopy. In their study, calcite

($CaCO_3$), ikaite ($CaCO_3.6H_2O$) and Amorphous Calcium Carbonate (ACC) show an

NMR signature at 168 ppm. For other crystalline materials (aragonite, vaterite, $CaCO_3$;

monohydrocalcite, $CaCO_3.H_2O$), the resonance is observed above that value at ppm shifts

from 169 to 171 ppm.

The assignment for the component at 177 ppm which is only observed with $\{^1H\}$ ^{13}C

CPMAS experiments is much more difficult to apprehend as only little information is

currently available for ^{13}C chemical shift above 170 ppm. We know this carbonate unit i)

is in very low quantity as it is not observed in ^{13}C Direct NMR, ii) is a high hydrogenated

environment as it is greatly enhanced in $\{^1H\}$ ^{13}C CPMAS experiments, iii) has a

distance between the carbonate molecule and the surrounding hydrogen atoms very short

compared to the carbonate unit at 167 ppm for which the peak intensity decreases as the

ct for CPMAS experiment is decreased, and iv) is directly correlated to the reduction

process as it is mainly enhanced in the most reduced samples. Our assignment is

supported by the following lines of evidence.

$\{^1H\}$ ^{13}C CPMAS experiments from Nebel et al. (2008) did not detected ^{13}C chemical

shift above 171 ppm which is the maximum noticed for vaterite. Thus, it is likely that 177

ppm component is not correlated to calcium.

There is an apparent correlation between the distortion of the carbonate environment and

the ^{13}C chemical shift. The more distorted is the carbonate group, the lower the ^{13}C

chemical shift is (Brooker et al., 1999; Kohn et al., 1991). We find the highly distorted

Si-carb.-Si at 155 ppm then followed by Si-carb.-Al at 160 ppm and Al-carb.-Al at 165

ppm. The identified component at 177 ppm should therefore be less distorted than those network units and even less distorted than the NBO-carb. Ca^{2+} proposed at 167 ppm. Ab initio molecular orbital calculations conducted by Tossell (1995) suggest that ^{13}C δ_{iso} above 170 ppm can be attributed to very peculiar carbonate unit: "ionic" clusters. In particular, a δ_{iso} at 177 ppm has been calculated for a "ionic" cluster composed of a Na^+ cation coordinated to a CO_2 molecule which is weakly bonded to an oxygen bridging 2 AlO_4 tetrahedron.

Based on the above evidence, one possible assignment for the 177 ppm component is to a "ionic" carbonate cluster such as the one described by Tossel (1995) or Kubicki and Stolper (1995): $BO-CO_2$ M^{n+}. We do not currently know the kind of charge compensating cation (M^{n+}). We state that Ca^{2+} is probably not a good candidate and instead Na^+ or Mg^{2+} should be considered. There is also a large incertitude on the aluminosilicate network units connected by the BO. The assignment proposed for the 177 ppm component is questionable. Therefore, it appears important to carry out more work in order to better constrain the carbonate environment in silicate melts.

     5.2 Modeling isobaric CO_2-H_2O solubility trend lines as a function of fO_2:

CO_2-H_2O solubility trend lines are shown in Figure 10 along with the CO_2 and H_2O analytical results we have obtained. The solid lines represent the isobaric CO_2-H_2O solubility trends for 150, 200, 250 and 300 MPa. The positions of the solid lines were calculated from solubility model established by Dixon et al (1995).

In the most oxidized sample, 6-1-*ox* (ΔFMQ+2.6), the solubility for CO_2 and H_2O is in excellent agreement with the calculated solubility model at 300 MPa. This is consistent

39

with the fact that in 6-1-*ox* the basaltic melt equilibrated with a fluid phase only

constituted by a binary mixture of CO_2 and H_2O (i.e. no other species are present).

On the contrary, the other samples solubility results depart significantly from the

calculated trends either at 200 MPa for 1-1-*200* or at 300 MPa for the other samples. For

samples synthesized at 300 MPa and under reducing conditions at roughly ΔFMQ-1.8,

the CO_2-H_2O solubility data are equivalent to the isobaric CO_2-H_2O trend at 250 MPa

according to the model of Dixon et al. (1995). Under more severe reducing conditions at

ΔFMQ-2.6, the CO_2-H_2O solubility falls on the isobaric line at 150 MPa from Dixon et

al. (1995).

The reducing conditions experienced by the samples are obviously responsible for this

downward displacement of dissolved CO_2 content. As stressed above, under reducing

conditions, the fluid phase during the experiment cannot be considered anymore as a

binary mixture of CO_2 and H_2O, instead, CO_2 is progressively replaced by CO (40 mol%

in 7-1-*red*, see Table 1). The system becomes at least ternary (CO_2-H_2O-CO) but can be

even more complex if we consider the presence of other reduced species such as CH_4 or

H_2. The obtained datum for reduced samples is systematically lower in CO_2 solubility

compared to 6-1-*ox* synthesized under oxidizing conditions. This result suggests that 1)

the addition of CO reduces the CO_2 solubility but also 2) that CO is almost not soluble

into basaltic melt which is consistent with the previous study of Pawley et al. (1992)

under drier conditions (<0.7 wt.% H_2O). Most of the data are consistent with the

described approach: however 3 points with fO_2 at ΔFMQ-1.2, -0.7 and -0.1 fall out of

such a general trend. This discrepancy can in large part be accounted for by 1) moderate

changes in experimental conditions, in particular the pressure of synthesis, 5-1 at ΔFMQ-

0.7 has an equilibrium pressure of 320 MPa which explains its slightly higher CO_2

content relative to other data; 2) possible analytical uncertainties using FTIR

spectroscopy for CO_2 quantification; and 3) the 3 charges are all characterized by

elevated H_2O content, hence it is possible that another mechanism of CO_2 solution plays a

role. For example, the high water content of those 3 particular samples may change the

CO_2 solubility trends as proposed by Behrens et al. (2009) for ultra-potassic magmas.

Aside from those second order effects, our results thus show that, as in H_2O-poor basaltic

liquids (Pawley et al., 1992), reduced hydrous basaltic liquids also display a decrease in

their CO_2 solubility compared to more oxidizing conditions. This decrease could be even

more dramatic if fO_2 conditions more reducing were to be applied.

5.3 CO_2 solubility versus CO_2 fugacity (fCO_2):

The evolution of CO_2 solubility as a function of fCO_2 is represented in Figure 11. Our

results (*open circle*) are compared to several other authors' data and for different

compositions ranging from rhyolite to basalt compositions. Our data points are also

additionally reported in a wider scale plot placed within the Figure 11 for additional

details. The H_2O^{tot} is given for each point alongside.

Altogether, our study is in agreement with the general trend showing the increase in CO_2

solubility with increasing fCO_2 in the fluid phase, as can be predicted from

thermodynamic arguments (e.g. Fogel and Rutherford, 1990; Dixon, 1997; Papale, 1999;

Behrens et al., 2004; Papale et al., 2006). Yet, at a given fCO_2, our results appear to be

slightly but systematically lower than in other studies.

We observe different trends depending on composition. The dataset for andesite is significantly higher than the other compositions represented here. The data on alkali-basalt (not represented here for clarity) from Botcharnikov et al. (2005) is even higher than andesite.

The results for our Fe-free synthetic glass are lower than the CO_2 solubility for rhyolite glass for example. This observation might reflect differences in the used extinction coefficients for CO_2 quantification by FTIR. We used a value of 69500 $L.mol^{-1}.cm^{-2}$ from Fine and Stolper (1986) which is valid for basaltic glass. However, our composition is Fe-free therefore the extinction coefficient value is only approximate in CO_2 quantification for our synthetic composition.

In the detailed plot, despite some scatter, H_2O rich melts appears to be those enriched in CO_2 relative to those H_2O poor, in qualitative agreement with early suggestions that an increase in melt H_2O content leads to an increase in CO_2 solubility (see for instance Behrens et al., 2009).

All data points are represented in Figure 11 regardless of fO_2. The lowest value is given by 1-1-*200* (FMQ-2.3). 6-1-*ox* (FMQ+2.6) lies in the highest part of the trend. At first sight, lowering the fO_2 will act primarily on the fluid phase composition increasing the ratio between CO and CO_2 and thus leading to fCO_2 decrease.

5.4 Implications of fO_2 reducing conditions for magmatic degassing in primitive planetary bodies, the Earth and Mars:

Considering that the Earth and Mars interiors may have experienced very reducing conditions, in particular during the first stages of their geological evolution (e.g. Righter

et al., 2007), our data confirm that, for comparable bulk C content of the mantle, at low fO_2 (i.e. at IW), larger amount of C-species may have degassed due to the combined effects of lower fCO_2 and insoluble character of CO, regardless of the dry or wet status of the magma ocean (see Gaillard and Scaillet, 2009).

We also show that under the reducing conditions investigated (from $\Delta IW-2$ to $+1$) other species than CO_2 are present in the fluid phase such as CO or even H_2. The presence of those reduced species will influence greatly for the modeling of the magma ocean degassing. Recent work by Elkins-Tanton (2008) modeled the outgassed flux of CO_2 produced by the solidification of the primitive magma ocean with application to Mars (and the early Earth), but such an estimate is based on the assumption only CO_2 is degassed during the crystallization of the magma ocean. However, the impact of CO release in the atmosphere cannot be neglected. For instance, at $\Delta FMQ-2.6$ (equivalent to $\Delta IW+1.1$), the X(CO) in the fluid phase represents 43 mol% (see Table 1). Prather (1996) and Daniel and Solomon (1998) showed that an intense release of CO in the atmosphere can induce a severe greenhouse effect through photochemical reaction producing on a short time scale CH_4 and O_3 gases. In fact, the indirect radiative forcing of CO on global warming appears more important than the CO_2 effect. Recent work by Kawaragi et al. (2009) showed that CO will produce an increase in the surface temperature which is probably 2 times the effect of CO_2 hence provoking major environmental changes.

6. Summary:

We have conducted an experimental investigation on the C-H-O fluid solubility and speciation in silicate melts as a function of redox conditions from moderately oxidized

(ΔFMQ+2.6) to reduced (ΔFMQ-2.6) conditions which are considered relevant to the Earth and Mars degassing.

Spectroscopic results suggest that C-H-O is dissolved as 3 main species: CO_3^{2-}, OH^- and H_2O^{mol}. The presence of carbonate units is consistent with dissolution mechanism model for basaltic glasses. We do not observe the presence of more reduced species such as CH_4.

Volatile species were quantified by FTIR. The CO_2 solubility is directly proportional to the fCO_2 in agreement with thermodynamic modeling. On the other hand, the CO_2 solubility is correlated to the fluid phase composition. On the contrary, the reduction of the aluminosilicate melt does not seem to play a major role into the CO_2 solubility trend. CO_2 solubility is strongly affected by redox conditions. CO_2 solubility measured in oxidized glass is in agreement with thermochemical modeling for isobaric CO_2-H_2O solubilities. Under reducing conditions, CO_2 solubility departs from thermochemical equilibrium and the CO_2-H_2O solubility trends as established at high fO_2. Our study shows that the presence of water does not lead to an increase in the solubility of "insoluble" species such as CO or CH_4, as compared to their behaviour under nominally dry conditions. Overall, our experimental results provide additional constraints for modeling the degassing of primitive interiors for Mars or the Earth. Future modeling should take into account the presence of reduced species (i.e., CO) into the fluid phase as an important part of the degassing processes which is likely to modify estimates so far done on the primitive atmosphere compositions.

Examination of carbonate environments presumes the existence of one main unit determined by ^{13}C-MAS NMR but an additional second component is revealed when

acquisition is performed with $\{^1H\}$ ^{13}C-CPMAS sequence. This unit is strongly enhanced in the most reduced samples. Dynamic CPMAS measurements also suggest a very close proximity of hydrogen atoms to this carbonate unit compared to the main carbonate unit. A possible assignment is proposed for the two components but remains hypothetical. The chemical shift values are in favor to carbonate groups NBO-carb. Ca^{2+} for 167 ppm and "ionic" carbonate groups $BO-CO_2$ M^{n+} for 177 ppm where M is a charge compensating cation such as Mg^{2+} or Na^+. More work is however to be conducted to confirm this point. Based on the study of the CO_2 solubility and speciation data, we suggest that applying reducing conditions to the fluid phase does not change dramatically the dissolution mechanisms for C species in hydrous melts; hence under moderately reducing conditions we do not possess evidence for a depolymerization or polymerization process of the melt with C-H-O species dissolution mechanisms.

References list:

Ahrens, T.J., 1989. Planetary origins – Water storage in the mantle. Nature 342, 122-123.

Azbel I.Y., and Tolstikhin, I.N., 1990. Geodynamics, magmatism and degassing of the Earth. Geochimica Cosmochimica Acta 54, 139-154.

Behrens, H., and Gaillard, F., 2006. Geochemical aspects of melts: Volatiles and redox behavior. Elements 2, 275-280.

Behrens, H., Ohlhorst, S., Holtz, F., and Champenois, M., 2004. CO_2 solubility in dacitic melts equilibrated with H_2O-CO_2 fluids: Implications for modeling the solubility of CO_2 in silicic melts. Geochimica Cosmochimica Acta 68, 4687-4703.

Behrens, H., Roux, J., Neuville, D.R., and Siemann, M., 2006. Quantification of dissolved H_2O in silicate glasses using confocal microRaman spectroscopy. Chemical Geology 229, 96-112.

Behrens, H., Misiti, V., Freda, C., Vetere, F., Botcharnikov, R.E., and Scarlato, P., 2009. Solubility of H_2O and CO_2 in ultrapotassic melts at 1200 and 1250°C and pressure from 50 to 500 MPa. American Mineralogist 94, 105-120.

Blank, J.G., and Brooker, R.A., 1994. Experimental studies of carbon dioxide in silicate melts: solubility, speciation and stable carbon isotope behaviour. In: Volatiles in magmas. Review in mineralogy (eds. Carroll M.R., Holloway, J.R.). Mineralogical Society of America, Washington, DC, 30, pp 157-186.

Botcharnikov, R.E., Freise, M., Holtz, F., and Behrens, H., 2005. Solubility of C-O-H mixtures in natural melts: new experimental data and application range of recent models. Annals of Geophysics 48, 634-646.

Botcharnikov, R.E., Behrens, H., and Holtz, F., 2006. Solubility and speciation of C-O-H fluids in andesitic melt at T=1100-1300°C and P=200 and 500MPa. Chemical Geology 229, 125-143.

Brooker, R.A., Kohn, S.C., Holloway, J.R., McMillan, P.F., and Carroll, M.R., 1999. Solubility, speciation and dissolution mechanisms for CO_2 in melts on the $NaAlO_2$-SiO_2 join. Geochimica Cosmochimica Acta 63, 3549-3565.

Brooker, R.A., Kohn, S.C., Holloway, J.R., and McMillan, P.F., 2001b. Structural controls on the solubility of CO_2 in silicate melts. Part II: IR characteristics of carbonate groups in silicate glasses. Chemical Geology 174, 241-254.

Burke E.A.J., 2001. Raman microspectrometry of fluid inclusions. Lithos 55, 139-158.

Cody, G.D., Mysen, B.O., and Lee, S.K., 2005. Structure vs. composition: A solid-state ^{1}H and ^{29}Si NMR study of quenched glasses along the Na_2O-SiO_2-H_2O join. Geochimica Cosmochimica Acta 69, 2373-2384.

Daniel, J.S., and Solomon, S., 1998. On the climate forcing of carbon monoxide. Journal of Geophysical Research 103 (D11), 13249-13260.

Di Carlo, I., Pichavant, M., Rotolo, S.G., and Scaillet, B., 2006. Experimental crystallization of a high-K arc basalt: The golden pumice, Stromboli volcano (Italy). Journal of Petrology 47, 1317-1343.

Dingwell, D.B., Hess, K.-U., and Romano, C., 1998. Viscosity data for hydrous peraluminous granitic melts: Comparison with a metaluminous model. American Mineralogist 83, 236-239.

Dixon, J.E., 1997. Degassing of alkalic basalts. American Mineralogist 82, 368-378.

Dixon, J.E., Stolper, E.M., and Holloway, J.R., 1995. An experimental study of water and carbon dioxide solubilities in Mid-Ocean Ridge Basaltic liquids. Part I: Calibration and solubility models. Journal of Petrology 36, 1607-1631.

Drake, M.J., and Righter, K., 2002. Determining the composition of the Earth. Nature 416, 39-44.

Elkins-Tanton, L. 2008. Linked magma ocean solidification and atmospheric growth Earth and Mars. Earth Planetary Science Letter 271, 181-191.

Eugster, H.P., and Wones, D.R., 1962. Stability relations of the ferruginous biotite, annite. Journal of Petrology 3, 82-125.

Fine, G., and Stolper, E., 1986. Dissolved carbon dioxide in basaltic glasses: concentrations and speciation. Earth Planetary Science Letter 76, 263-278.

Fogel, R.A., and Rutherford, M.J., 1990. The solubility of carbon dioxide in rhyolitic melts: A quantitative FTIR study. American Mineralogist 75, 1311-1326.

Frantz, J.D., and Mysen, B.O., 1995. Raman spectra and structure of $BaO\text{-}SiO_2$, $SrO\text{-}SiO_2$ and $CaO\text{-}SiO_2$ melts to 1600°C. Chemical Geology 121, 155-176.

Fung, B.M., Khitrin, A.K., and Ermolaev, K., 2000. An improved broadband decoupling sequence for liquid crystals and solids. Journal of Magnetic Resonance 142, 97-101.

Gaillard, F., Schmidt, B.C., Mackwell, S., and McCammon C., 2003a. Rate of hydrogen-iron redox exchange in silicate melts and glasses. Geochimica Cosmochimica Acta 67, 2427-2441.

Gaillard, F., Pichavant, M., and Scaillet, B., 2003b. Experimental determination of activities of FeO and Fe_2O_3 components in hydrous silicic melts under oxidizing conditions. Geochimica Cosmochimica Acta 67, 4389-4409.

Gaillard, F., Malki, M., Iacono-Marziano, G., Pichavant, M., and Scaillet, B., 2008. Carbonatite melts and electrical conductivity of the asthenosphere. Science 322, 1363-1365.

Gaillard, F., and Scaillet, B., 2009. The sulfur content of volcanic gases on Mars. Earth Planetary Science Letter 279, 34-43.

Giordano, D., Russell, J.K., and Dingwell, D.B., 2008. Viscosity of magmatic liquids: A model. Earth Planetary Science Letter 271, 123-134.

Hahn, E.L., 1950. Spin Echoes. Physical Review 80, 580-594.

Hirschmann, M.M., and Withers, A.C., 2008. Ventilation of CO_2 from a reduced mantle and consequences for the early Martian greenhouse. Earth Planetary Science Letter 270, 147-155.

Holland, T., and Powell, R., 1991. A Compensated-Redlich-Kwong (CORK) equation for volumes and fugacities of CO_2 and H_2O in the range 1bar-50kbar and 100-1600°C. Contribution to Mineralogy and Petrology 109, 265-273.

Iacono-Marziano, G., Gaillard, F., and Pichavant, M., 2008. Limestone assimilation by basaltic magmas: an experimental re-assessment and application to Italian volcanoes. Contribution to Mineralogy and Petrology 155, 719-738.

Ihinger, P.D., Hervig, R.L., and McMillan, P.F., 1994. Analytical methods for volatiles in glasses. In: Volatiles in magmas. Review in mineralogy (Carroll M.R., Holloway J.R., Eds.) Mineral. Soc. Am., Washington, DC, 30, pp 67-121.

Ingrin, J., Hercule, S. and Charton, T., 1995. Diffusion of hydrogen in diopside: Results of dehydration experiments. Journal of Geophysical Research 100, 15489-15499.

Javoy, M., Stillman, C.J., and Pineau, F., 1986. Oxygen and hydrogen isotope studies on the basal complexes of the Canary-Islands – implications on the conditions of their genesis. Contribution to Mineralogy and Petrology 92, 225-235.

Jones, A.R., Winter, R., Greaves, G.N., and Smith, I.H., 2005. ^{23}Na, ^{29}Si, and ^{13}C MAS NMR investigation of glass-forming reactions between Na_2CO_3 and SiO_2. Journal of Physical Chemistry B, 109, 23154-23161.

Kadik, A., Pineau, F., Litvin, Y., Jendrzejewski, N., Martinez, I., and Javoy, M., 2004. Formation of Carbon and Hydrogen species in magmas at low oxygen fugacity. Journal of Petrology 45, 1297-1310.

Kawaragi, K., Sekine, Y., Kadono, T., Sugita, S., Ohno, S., Ishibashi. K., Kurosawa, K., Matsui, T., and Ikeda, S., 2009. Direct measurements of chemical composition of shock-induced gases from calcite: an intense global warming after Chicxulub impact due to the

indirect greenhouse effect of carbon monoxide. Earth Planetary Science Letter 282, 56-64.

King, P.L., and Holloway, J.R., 2002. CO_2 solubility and speciation in intermediate (andesitic) melts: The role of H_2O and composition. Geochimica Cosmochimica Acta 66, 1627-1640.

King, P.L., Vennemann, T.W., Holloway, J.R., Hervig, R.L., Lowenstern, J.B., and Forneris, J.F., 2002. Analytical techniques for volatiles: A case study using intermediate (andesitic) glasses. American Mineralogist 87, 1077-1089.

Khimyak, Y.Z., and Klinowski, J., 2001. Solid-state NMR studies of the organic template in mesostructured aluminophosphates. Physical Chemistry and Chemical Physics 3, 616-626.

Kohn, S.C., Brooker, R.A., and Dupree, R., 1991. ^{13}C MAS NMR: A method for studying CO_2 speciation in glasses. Geochimica Cosmochimica Acta 55, 3879-3884.

Kubicki, J.D., and Stolper, E.M., 1995. Structural roles of CO_2 and $[CO_3]^{2-}$ in fully polymerized sodium aluminosilicate melts and glasses. Geochimica Cosmochimica Acta 59, 683-698.

Kump, L.R., 2008. The rise of atmospheric oxygen. Nature 451, 277-278.

Kump, L.R., and Barley, M. E., 2007. Increased subaerial volcanism and the rise of atmospheric oxygen 2.5 billion years ago. Nature 448, 1033-1036.

Lange, R.A., and Carmichael, I.S.E., 1987. Densities of Na_2O-K_2O-CaO-MgO-FeO-Fe_2O_3-Al_2O_3-TiO_2-SiO_2 liquids: new measurements and derived partial molar properties. Geochimica Cosmochimica Acta 53, 2195-2204.

Laws, D.D., Bitter, H.M.L., and Jerschow, A., 2002. Solid-state NMR spectroscopic methods in chemistry. Angewandte Chemie International Edition 41, 3096-3129

Lesne, P., Scaillet, B., Pichavant, M., and Beny, J.-M., subm. The carbon dioxide solubility in alkali basalts: and experimental study. Contribution to Mineralogy and Petrology.

London, D., 1992. Phosphorous in S-type magmas: The P_2O_5 content of felspars from peraluminous granites, pegmatites, and rhyolites. American Mineralogist 77, 126-145.

Long, D.A., 2002 The Raman effect: A unified treatment of the theory of Raman scattering by molecules. (John Wiley and Sons Eds) pp. 598.

Maekawa, H., Maekawa, T., Kawamura, K., and Yokokawa, T., 1991. The structural groups of alkali silicate glasses determined from ^{29}Si MAS NMR. Journal of Non-Crystalline Solids 127, 53-64.

Mandeville, C.W., Webster, J.D., Rutherford, M.J., Taylor, B.E., Timbal, A., and Faure, K., 2002. Determination of molar absorptivities for infrared absorption bands of H_2O in andesitic glasses. American Mineralogist 87, 813-821.

Martel, C., Pichavant, M., Holtz, F., Scaillet, B., Bourdier, J.-L., and Traineau, H., 1999. Effects of $f(O_2)$ and H_2O on andesite phase relations between 2 and 4 kbar. Journal of Geophysical Research Solid Earth 104, 29453-29470.

Marty, B., and Jambon, A., 1987. C/3He in volatile fluxes from the solid Earth – Implications for carbon geodynamic. Earth Planetary Science Letter 83, 16-26.

Mercier, M., Di Muro, A., Giordano, D., Métrich, N., Lesne, P., Pichavant, M., Scaillet, B., and Clocchiatti, R., 2009. Influence of glass polymerisation and oxidation on micro-Raman water analysis in alumino-silicate glasses. Geochimica Cosmochimica Acta 73, 197-217.

Moore, G., 2008. Interpreting H_2O and CO_2 contents in melt inclusions: Constraints from solubility experiments and modeling. In: Minerals, Inclusions and Volcanic processes.

Review in mineralogy and geochemistry (Putirka K.D. and Tepley III F.J., Eds.) Mineral. Soc. Am., Washington, DC, 69, pp 333-361.

Morizet, Y., Kohn, S.C., and Brooker, R.A., 2001. Annealing experiments on CO_2-bearing jadeite glass: an insight into the true temperature dependence of CO_2 speciation in silicate melts. Mineralogical Magazine 65, 701-707.

Morizet, Y., Brooker, R.A., and Kohn, S.C., 2002. CO_2 in haplo-phonolite Melt: Solubility, speciation and carbonate complexation. Geochimica Cosmochimica Acta 66, 1809-1820.

Morizet, Y., Paris, M., Gaillard, F., and Scaillet, B., 2009. Raman quantification factor calibration for $CO-CO_2$ gas mixture in synthetic fluid inclusions: Application to oxygen fugacity calculation in magmatic systems. Chemical Geology 264, 58-70.

Mysen, B.O., 1988. Structure and properties of silicate melts. In: Development in Geochemistry, vol. 4. Elsevier, Amsterdam, 354 pp.

Mysen, B.O., 1990. Effect of pressure, temperature and bulk composition on the structure and species distribution in depolymerised alkali aluminosilicate melts and quenched melts. Journal of Geophysical Research B 95, 15733-15744.

Mysen, B.O., Fogel, M.L., Morrill, P.L., and Cody, G.D., 2009. Solution behavior of reduced C-O-H volatiles in silicate melts at high pressure and temperature. Geochimica Cosmochimica Acta 73, 1696-1710.

Nebel, H.N.M., Mayer, C., and Epple, M., 2008. On the structure of amorphous calcium carbonate - A detailed study by solid-state NMR spectroscopy. Inorganic Chemistry 47, 7874-7879.

Nowak, M., Probatzki, D., Spickenbom, K., and Diedrich., O., 2003. Carbon dioxide speciation in silicate melts: a restart. Earth and Planetary Science Letters 207, 131-139.

Okomura, S., Nakamura, M., and Nakashima, S., 2003. Determination of molar absorptivity of IR fundamental OH-stretching vibration in rhyolitic glasses. American Mineralogist 88, 1657-1662.

Olhorst, S., Behrens, H., and Holtz, F. 2001. Compositional dependence of molar absorptivities of near-infrared OH- and H_2O bands in rhyolitic to basaltic glasses. Chemical Geology 174, 5-20.

Pan, V., Holloway, J.R., and Hervig, R., 1991. The pressure and temperature dependence of carbon dioxide solubility in tholeiitic basalt melts. Geochimica Cosmochimica Acta 55, 1587-1595.

Papale, P., 1999. Modeling of the solubility of a two-component $H_2O + CO_2$ fluid in silicate liquids. American Mineralogist 84, 477-492.

Papale, P., Moretti, R., and Barbato, D., 2006. The compositional dependence of the saturation surface of H_2O+CO_2 fluids in silicate melts. Chemical Geology 229, 78-95.

Papenguth, H.W., Kirkpatrick, R.J., Montez, B., and Sandberg, P.A., 1989. ^{13}C MAS NMR spectroscopy of inorganic and biogenic carbonates. American Mineralogist 74, 1152-1158.

Pawley, A.R., Holloway, J.R., and McMillan, P.F., 1992. The effect of oxygen fugacity on the solubility of carbon-oxygen fluids in basaltic melt. Earth Planetary Science Letter 110, 213-225.

Prather, M.J., 1996. Time scales in atmospheric chemistry: Theory, GWPs for CH_4 and CO, and runaway growth. Geophysical Research Letters 23, 2597-2600.

Puls, S.P., and Eckert, H., 2006. Site discrimination in mixed-alkali glasses studied by Cross-Polarization NMR. Journal of Physical Chemistry B 110, 14253-14261.

Righter, K., Drake, M.J., and Scott, E., 2007. Compositional relationships between meteorites and terrestrial planets. In: Meteorites and the Early Solar system II, (Lauretta D., Leshin L., McSween H.Y., Eds). Univ. Arizona Press, Tucson.

Ripmeester, J.A., and Ratcliffe, C.I., 1988. Low-temperature cross-polarisation/magic angle spinning ^{13}C NMR of solid methane hydrates: structure, cage occupancy, and hydration number. Journal of Physical Chemistry 92, 337-339.

Robert, E., Whittington, A., Fayon, F., Pichavant, M., and Massiot, D., 2001. Structural characterization of water-bearing silicate and aluminosilicate glasses by high-resolution solid-state NMR. Chemical Geology 174, 291-305.

Robie, R.A., and Hemingway, B.S., 1995. Thermodynamic Properties of Minerals and Related Substances at 298.15 K and 1 Bar (105 Pascals) Pressure and at Higher Temperatures, U.S. Geological Survey Bulletin 2131. U.S. GPO, Washington, DC.

Scaillet, B., Pichavant, M., Roux, J., Humbert, G., and Lefèvre, A., 1992. Improvements of the Shaw membrane technique for measurement and control of fH$_2$ at high temperatures and pressures. American Mineralogist 77, 647-655.

Scaillet, B., and Pichavant, M., 2004. Role of fO$_2$ on fluid saturation in oceanic basalt. Nature 430, DOI: 10.1038/nature02814|ISSN 0028-0836.

Schmidt, B.C., Holtz, F., Scaillet, B., and Pichavant, M., 1997. The influence of H$_2$O-H$_2$ fluids and redox conditions on melting temperatures in the haplogranite system. Contribution to Mineralogy and Petrology 126, 386-400.

Schmidt, B.C., Riemer, T., Kohn, S.C., Behrens, H., and Dupree, R., 2000. Different water solubility mechanisms in hydrous glasses along the Qz-Ab Join: Evidence from NMR Spectroscopy. Geochimica Cosmochimica Acta 64, 513-526.

Shi, P., and Saxena, S.K., 1992. Thermodynamic modeling of the C-H-O-S fluid system. American Mineralogist 77, 1038-1049.

Silver, L.A., Ihinger, P.D., and Stolper, E., 1990. The influence of bulk composition on the speciation of water in silicate glasses. Contribution to Mineralogy and Petrology 104, 142-162.

Sleep, N.H., and Zahnle, K., 2001. Carbon dioxide cycling and implications for climate on ancient Earth. Journal of Geophysical Research – Planets 106, 1373-1399.

Spickenbom, K., Serrialta, M., and Nowak, M., 2010. Carbon dioxide and argon diffusion in silicate melts: insights into the CO_2 speciation in magmas. Geochimica Cosmochimica Acta, doi: 10.1016/j.gca.2010.08.022.

Stolper, E.M., (1982). Water in silicate glasses: an infrared spectroscopic study. Contribution to Mineralogy and Petrology 81, 1-17.

Stuke, A., Behrens, H., Schmidt, B.C., and Dupree, R., 2006. H_2O speciation in float glass and soda lime glass. Chemical Geology 229, 64-77.

Subramanian, S., Kini, R.A., Dec, S.F., and Sloan, E.D., 2000. Evidence of structure II hydrate formation from methane + ethane mixtures. Chemical Engineering. Science 55, 1981-1999.

Tamic, N., Behrens, H., and Holtz, F., 2001. The solubility of H_2O and CO_2 in rhyolitic melts in equilibrium with a mixed CO_2-H_2O fluid phase. Chemical Geology 174, 333-347.

Taylor, W.R., 1990. The dissolution mechanism of CO_2 in aluminosilicate melts − infrared spectroscopic constraints on the cationic environment of dissolved $[CO_3]^{2-}$. European Journal of Mineralogy 2, 547-563.

Taylor, R.E., 2004. Setting up ^{13}C CP/MAS experiments. Concepts in Magnetic Resonance Part A 22, 37–49

Thibault, Y., and Holloway, J.R., 1994. Solubility of CO_2 in a Ca-rich leucitite: effects of pressure, temperature and oxygen fugacity. Contribution to Mineralogy and Petrology 116, 216-224.

Thomas, R., Webster, J.D., and Heinrich, W., 2000. Melt inclusions in pegmatite quartz: complete miscibility between silicate melts and hydrous fluids at low pressure. Contribution to Mineralogy and Petrology 139, 394-401.

Tossell, J.A., 1995. Calculation of the ^{13}C NMR shieldings of the CO_2 complexes of aluminosilicates. Geochimica Cosmochimica Acta 59, 1299-1305.

Watson, E.B., 1994. Diffusion in volatile-bearing magmas. In: Volatiles in magmas. Review in mineralogy (Carroll M.R., Holloway J.R., Eds.) Mineral. Soc. Am., Washington, DC, 30, pp 371-411.

Withers, A.C., and Behrens, H., 1999. Temperature-induced changes in the NIR spectra of hydrous albitic and rhyolitic glasses between 300 and 100 K. Physic and Chemistry of Minerals 27, 119-132.

Xue, X., and Kanzaki, M., 2004. Dissolution mechanisms of water in depolymerised silicate melts: constraints from ^{1}H and ^{29}Si NMR spectroscopy and ab initio calculations. Geochimica Cosmochimica Acta 68, 5027-5057.

Yamashita, S., Behrens, H., Schmidt, B.C., and Dupree, R., 2008. Water speciation in sodium silicate glasses based on NIR and NMR spectroscopy. Chemical Geology 256, 231-241.

Zajacz, Z., Halter, W., Malfait, W.J., Muntener, O., Bodnar, R.J., Bahcmann, O., Webster, J.D., Ulmer, P., Mandeville, C.W., Hirschmann, M.M. and Morizet, Y., 2005. A composition independent quantitative determination of the water content in silicate glasses and silicate melt inclusions by confocal Raman-spectroscopy. Contribution to Mineralogy and Petrology 150, 631-642.

Zeng, Q., Nekvasil, H., and Grey, C.P., 1999. Proton environments in hydrous aluminosilicate glasses: a ^{1}H MAS, ^{1}H/^{27}Al, and ^{1}H/^{23}Na TRAPDOR NMR study. Journal of Physical Chemistry B 103, 7406-7415.

Zhang, Y., and Zindler, A., 1989. Noble-gas constraints on the evolution of the Earth's atmosphere. Journal of Geophysical Research Solid Earth 94, 13719-13737.

Zhang, Y., Stolper, E.M., and Ihinger, P.D., 1995. Kinetics of the reaction $H_2O + O = 2OH$ in rhyolitic and albitic glasses: Preliminary results. American Mineralogist 80, 593-612.

Zhang, Y., Xu, Z., Mengfan, Z., and Wang H., 2007. Silicate melt properties and volcanic eruptions. Reviews of Geophysics 45, 216-242.

Zolotov, M.Y., and Fegley, B.Jr., 1999. Oxidation state of volcanic gases and the interior of Io. Icarus 141, 40-52.

Figure caption:

Figure 1: Log fO_2 (1) calculated from the H_2O^{tot} in the melt versus the log fO_2 (2) calculated from $X(CO_2)$-$X(CO)$ measured in fluid inclusions. The error on log fO_2 (1) was calculated considering an upper and lower value for H_2O^{tot} dissolved in the glass (± 0.20 wt.% H_2O as given in Table 3). The error on the log fO_2 (2) was 1) an upper and lower value for $X(CO_2)$-$X(CO)$ for fluid inclusions analyses. The 1:1 line is represented in dashed line.

Figure 2: Micro-Raman spectra for fluid inclusion analysis. A, CO_2 vibrational signatures for $2\nu_2$ and ν_1 and for both ^{12}C and ^{13}C isotopes between 1200 and 1500 cm^{-1}. The ΔFMQ conditions and the %^{13}C calculated from fluid inclusions and reported in Table 1 are indicated next to each spectrum. B, ^{12}CO and ^{13}CO vibrational signatures between 2000 and 2200 cm^{-1}. An intensity scaling factor of 2 was applied for better viewing. The CO_2 molar fraction calculated from fluid inclusions is also reported. C, Evidence for CH_4 in fluid inclusions. A scaling factor of 4 is applied to show the very low intensity of this species (calculated value indicated alongside).

Figure 3: Raman spectra obtained in the water vibrational region (2700-3900 cm^{-1}) and in the glass structure vibrational region (200-1250 cm^{-1}) showing 2 main vibrations: T-O stretching (800-1200 cm^{-1}) and T-O-T bending and rocking (300-700 cm^{-1}). A typical baseline is shown as dashed line underneath 6-1-*ox*. Spectra are uncorrected for black

body radiation. The H_2O^{tot} (2) is indicated next to each spectrum and has been calculated with Behrens et al. (2006) method.

Figure 4: FTIR spectra for glasses showing different ^{13}C enrichment calculated from fluid inclusions analysis: A, 80%; B, 40%; C, 1% ^{13}C. In all case the carbonates are represented by a peak doublet between 1400 and 1600 cm^{-1} corresponding to the antisymmetric stretching (ν_3). The $\Delta\nu_3$ remains constant with a value between 65 and 80 cm^{-1}. We reported next to each spectrum the ΔFMQ and ppm CO_2.

Figure 5: A, FTIR vibrational signature for OH^- groups (4500 cm^{-1}) and H_2O^{mol} (5200 cm^{-1}); B, FTIR vibrational signature for H_2O^{tot} (3500 cm^{-1}). The concentrations for each species is given next to each spectrum and reported in Table 3. All values indicated on A and B were calculated from Beer-Lambert law and using the extinction coefficients proposed by Stolper et al. (1982). The error on each concentration was determined from standard deviation on replicated FTIR analyses. A dashed line underneath each spectrum represents the baseline.

Figure 6: ^{13}C-MAS NMR spectra acquired with spin-echo sequence. Spectra show 3 main signatures: 125, 184 ppm for CO_2 and CO in the gaseous phase entrapped in fluid inclusions; broad signature between 155 and 170 ppm for carbonate groups dissolved in the glass. ΔFMQ and CO_2 content have been indicated for comparison. As a comparison, we included spectra from other studies: haplophonolite from Morizet et al. (2002) and sodamelilite from Kohn et al. (1991).

Figure 7: {^{1}H} ^{13}C-CPMAS NMR spectra acquired with 3.5 ms contact time for different samples. ΔFMQ and wt.% H_2O are given. One symmetric component is visible at 167 ppm for all samples. An additional broad carbonate group appears in the most reduced sample at 177 ppm.

Figure 8: {^{1}H} ^{13}C CPMAS spectra for 7-1-*red* (ΔFMQ-2.6) and 7-2 (ΔFMQ-1.2) obtained for different contact time (0.5, 1.0 and 3.5 ms) showing the change in carbonate environments within the glass. This dynamic study suggests a close proximity between hydrogen and carbon for the component at 177 ppm.

Figure 9: wt.% H_2O^{tot} determined from Micro-Raman analyses (H_2O^{tot} (2)) versus wt.% H_2O^{tot} determined from FTIR (see Table 3): ■, H_2O^{tot} (1) determined from the sum OH + H_2O^{mol}; ○ and ●, H_2O^{tot} determined from respectively the height and the area of the peak at 3500 cm^{-1}; Those data points were calculated using the extinction coefficients (ε) of Stolper et al. (1982). ▽, H_2O^{tot} determined from the height of the peak at 3500 cm^{-1} and using the extinction coefficient derived by Mandeville et al. (2002). 1:1 slope is represented with dashed line. Error on each point is given in Table 3 and determined from standard deviation and error propagation for FTIR value and an assumed error of ± 0.20 wt.% for on H_2O^{tot} (2) determined by Raman is taken.

Figure 10: ppm CO_2 versus wt.% H_2O. ΔFMQ value is indicated next to each point. ● are 300 MPa data, ○ is 200 MPa 1-1-*200* and ◇ is for 4-2-*us* nominally CO_2-free glass.

Solid lines are isobaric CO_2-H_2O solubility trends at 150, 200, 250 and 300 MPa obtained from thermochemical equilibrium of Dixon et al. (1995) and for relatively oxidized conditions.

Figure 11: ppm CO_2 versus $f$$CO_2$. Several dataset are represented in this plot: This study (*open circle*), rhyolite (Tamic et al., 2001; *filled triangle*); basalt (Pan et al., 1991; *inversed open triangle*; Pawley et al., 1992; *filled square*; Dixon et al., 1995; *filled diamond*; Botcharnikov et al., 2005; *filled hexagon*; Lesne et al., *subm.*; *stars*) and andesite (Botcharnikov et al., 2006; *open hexagon*). An insert is added to the plot with an increased scale showing only our data points with H_2O^{tot} indicated.
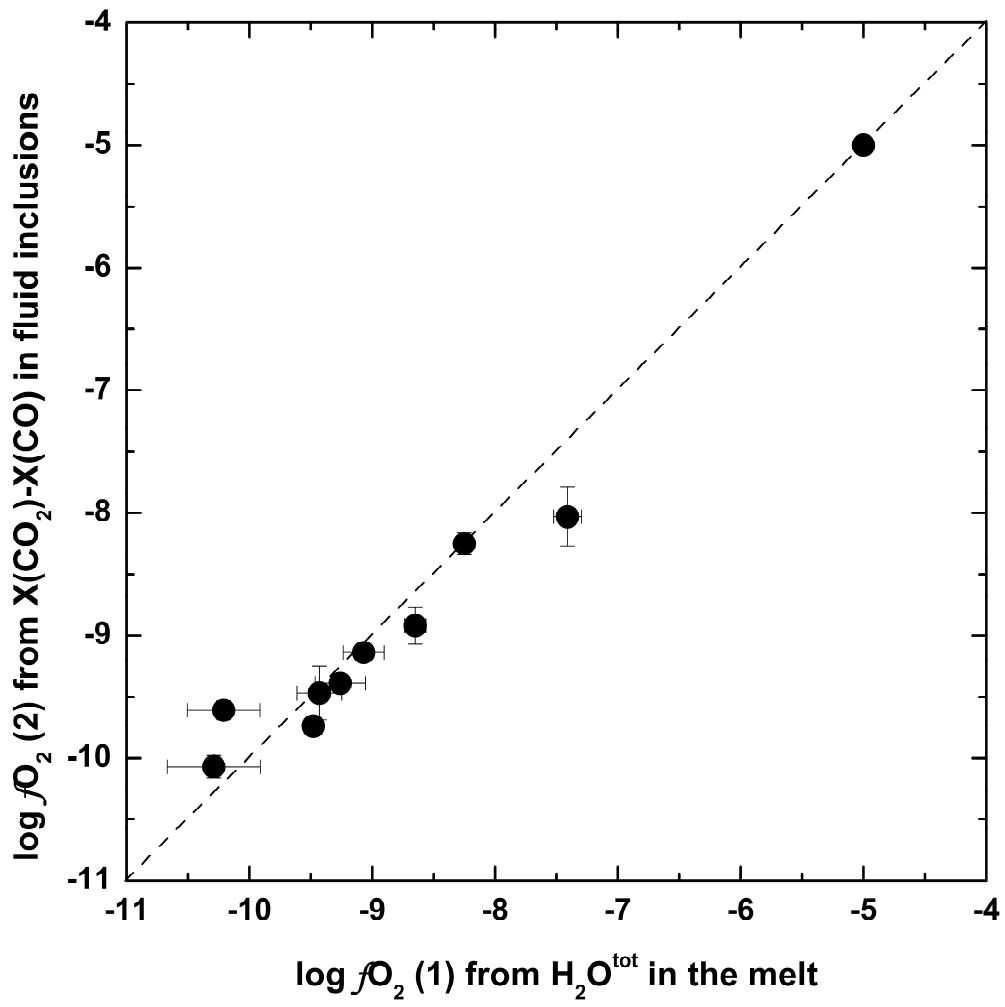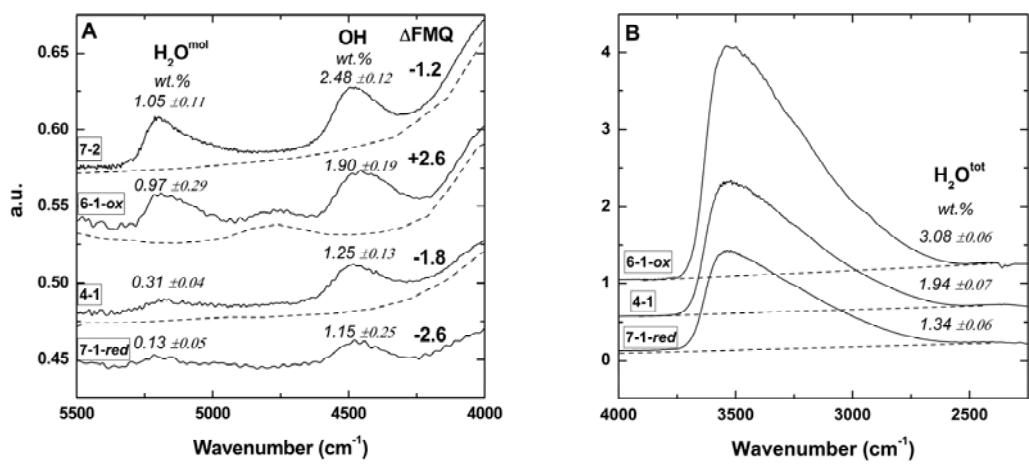
Figure 1
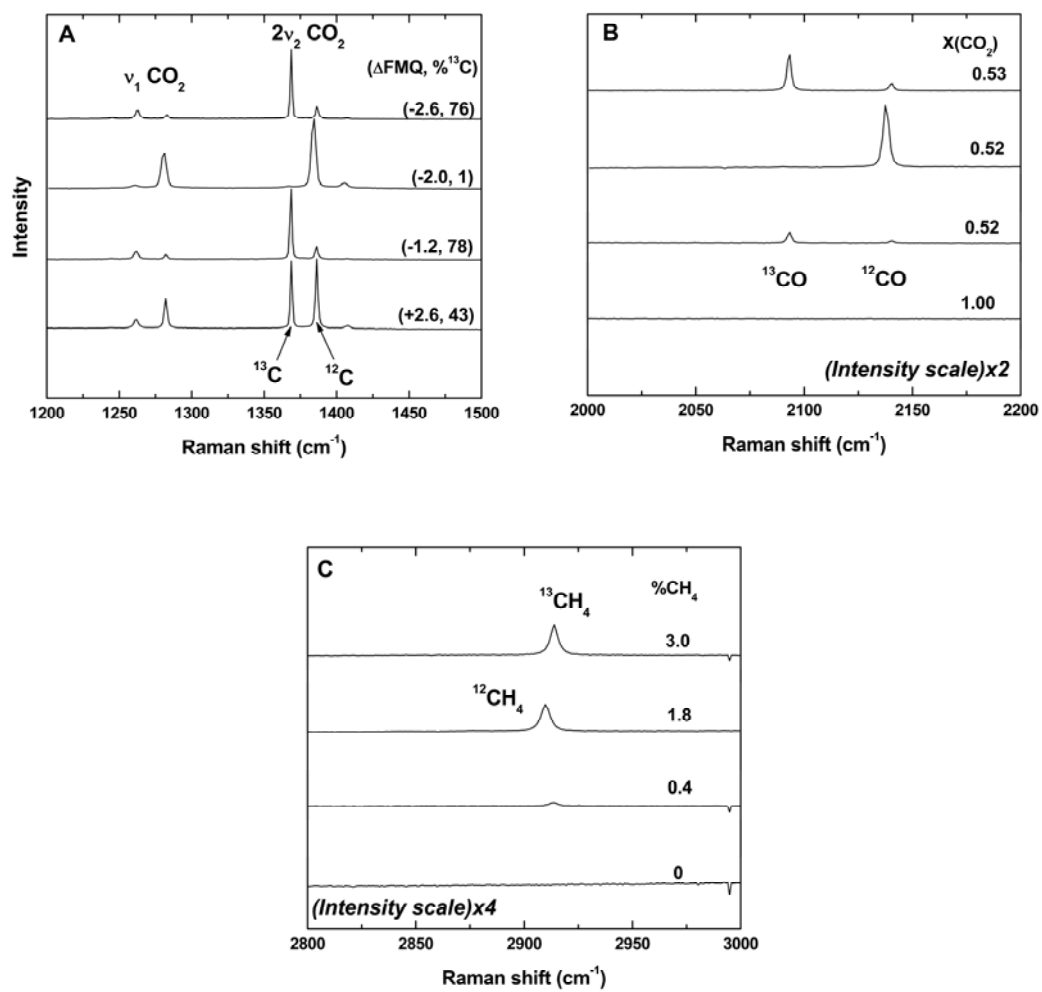
Figure 2
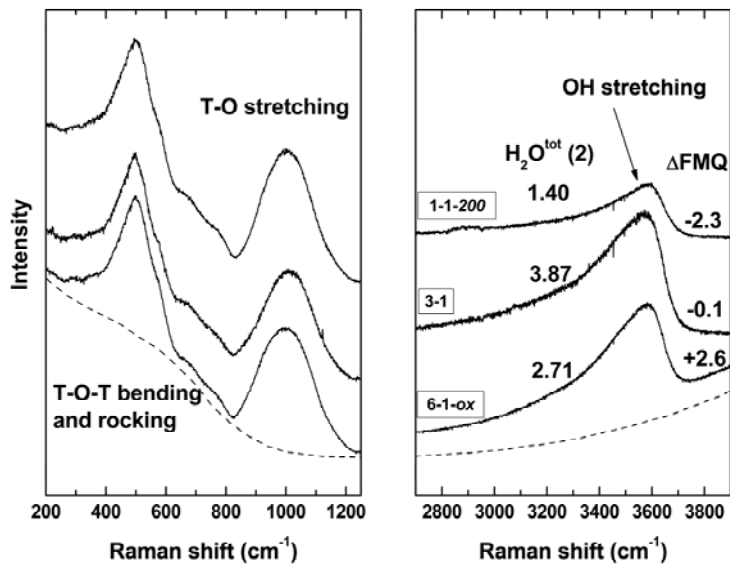
Figure 3
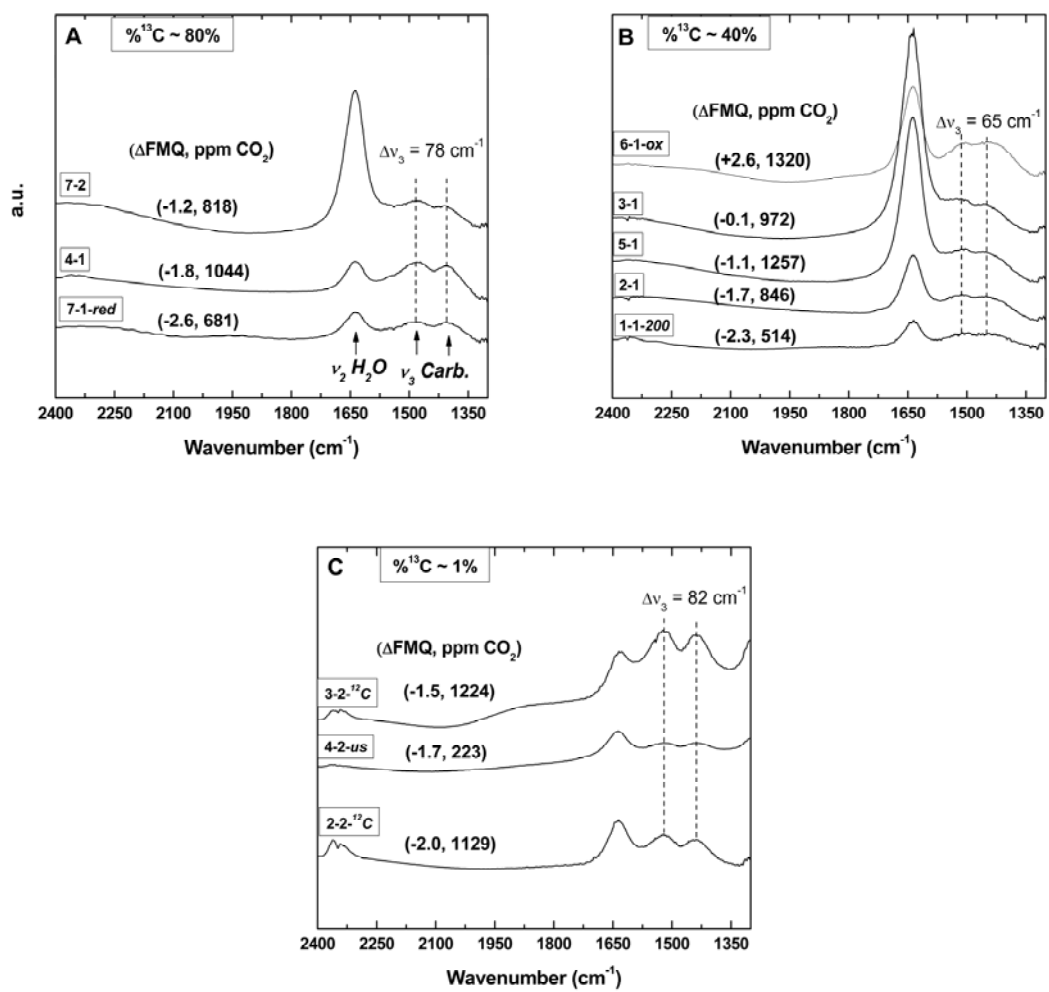
Figure 4

Figure 5

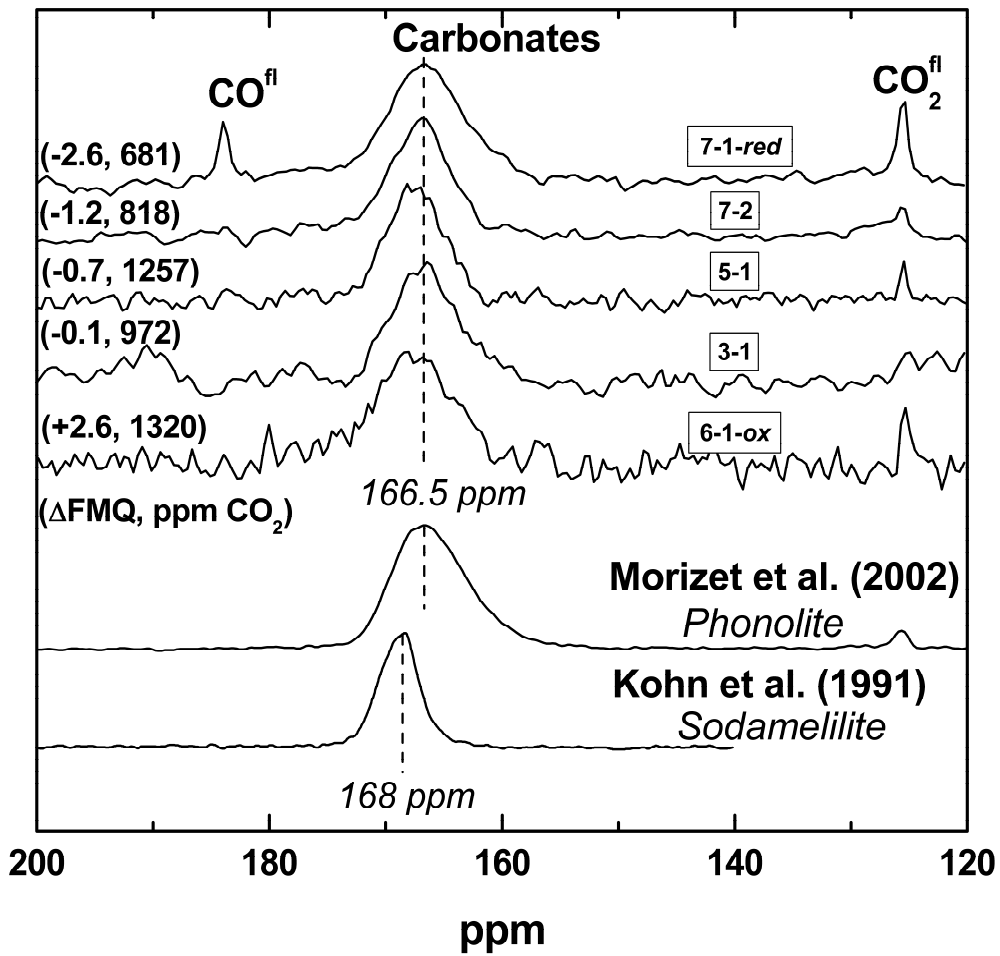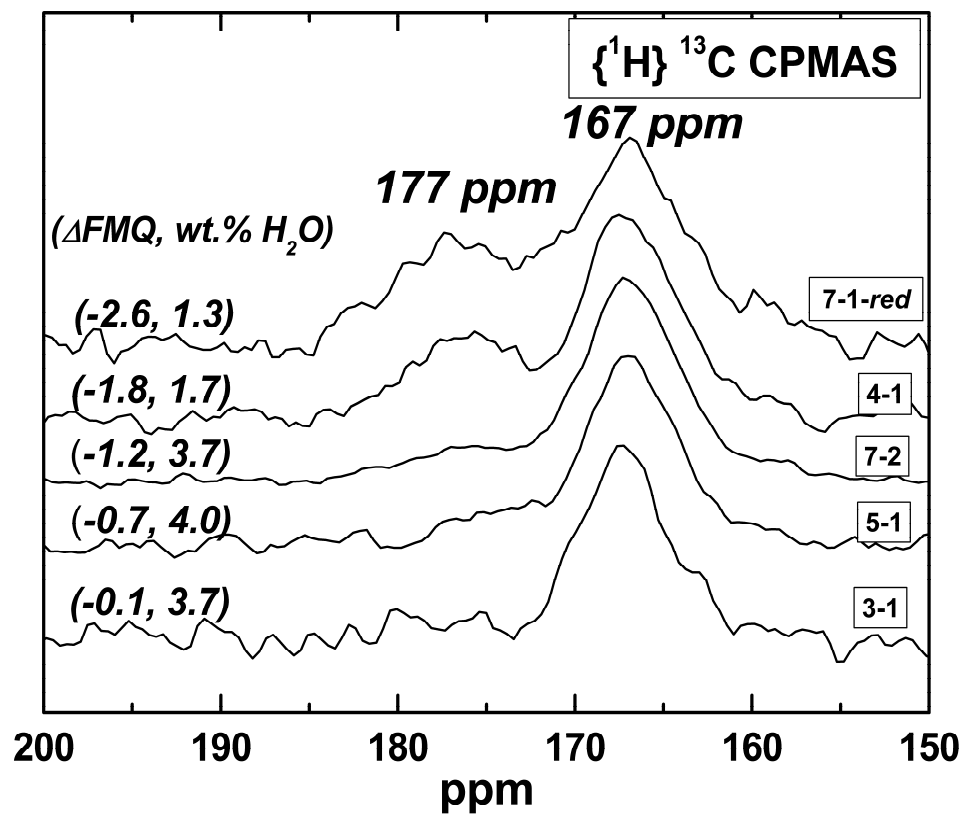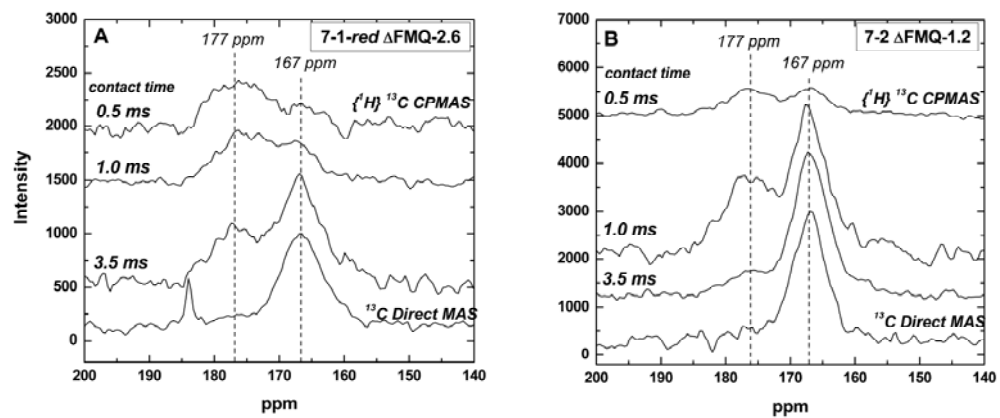Figure 6

Figure 7

Figure 8

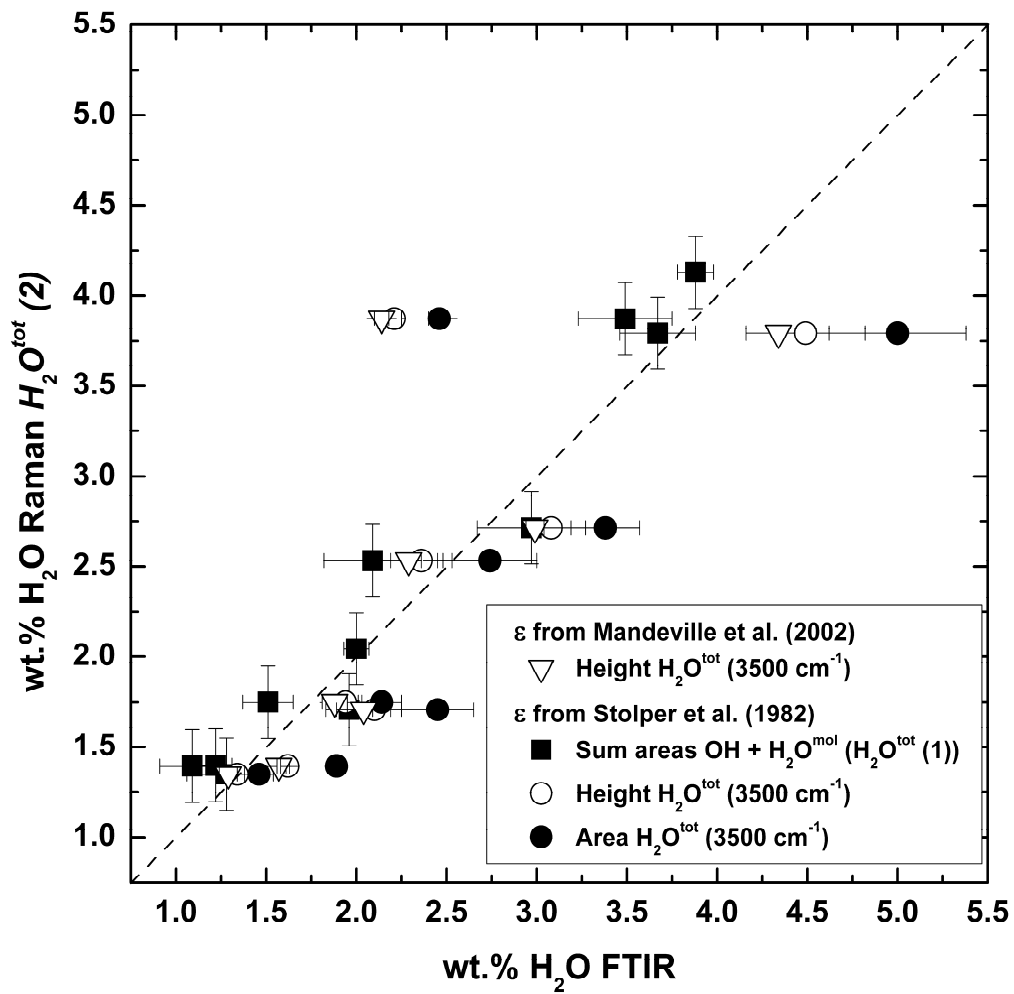The plot shows wt.% H_2O Raman H_2O^{tot} (2) on the y-axis versus wt.% H_2O FTIR on the x-axis.

Legend:
ε from Mandeville et al. (2002)
▽ Height H_2O^{tot} (3500 cm^{-1})
ε from Stolper et al. (1982)
■ Sum areas OH + H_2O^{mol} (H_2O^{tot} (1))
○ Height H_2O^{tot} (3500 cm^{-1})
● Area H_2O^{tot} (3500 cm^{-1})

Figure 9

Figure 10

Figure 11